

1 **This article is a preprint published at EarthArXiv**

2 **Notice - From the AMS Copyright Policy section 7c:**

3 This work has been submitted to the Journal of Climate. Copyright in this work may be
4 transferred without further notice. This work has not yet been peer-reviewed and is pro-
5 vided by the contributing author(s) as a means to ensure timely dissemination of schol-
6 arly and technical work on a noncommercial basis. Copyright and all rights therein are
7 maintained by the author(s) or by other copyright owners. It is understood that all per-
8 sons copying this information will adhere to the terms and constraints invoked by each au-
9 thor's copyright. This work may not be reposted without explicit permission of the copy-
10 right owner. [https://www.ametsoc.org/index.cfm/ams/publications/ethicalguidelines- and-ams-](https://www.ametsoc.org/index.cfm/ams/publications/ethicalguidelines-and-ams-policies/ams-copyright-policy)
11 [policies/ams-copyright-policy.](https://www.ametsoc.org/index.cfm/ams/publications/ethicalguidelines-and-ams-policies/ams-copyright-policy)

12 **Feedbacks on zonal mean tropical precipitation shifts induced by land**
13 **surface change**

14 Marysa M. Laguë*

15 *Department of Earth and Planetary Science, University of California, Berkeley, Berkeley, CA,*
16 *USA*

17 Abigail L. S. Swann

18 *Department of Atmospheric Sciences, University of Washington, Seattle, WA, USA*

19 *Department of Biology, University of Washington, Seattle, WA, USA*

20

William R. Boos

21

Department of Earth and Planetary Science, University of California, Berkeley, Berkeley, CA,

22

USA

23

Climate and Ecosystem Sciences Division, Lawrence Berkeley National Laboratory, Berkeley,

24

CA, USA

25

**Corresponding author address: Marysa M. Laguë, Department of Earth and Planetary Science,*

26

University of California Berkeley, 307 McCone Hall, Berkeley, CA 94720.

27

E-mail: mlague@berkeley.edu

ABSTRACT

28 Changes in land surface albedo and land surface evaporation modulate the
29 atmospheric energy budget by changing temperatures, water vapor, clouds,
30 snow and ice cover, and the partitioning of surface energy fluxes. Here ide-
31 alized perturbations to land surface properties are imposed in a global model
32 to understand how such forcings drive shifts in zonal mean atmospheric en-
33 ergy transport and zonal mean tropical precipitation. For a uniform decrease
34 in global land albedo, the albedo forcing and a positive water vapour feed-
35 back contribute roughly equally to increased energy absorption at the top of
36 the atmosphere (TOA), while radiative changes due to the temperature and
37 cloud cover response provide a negative feedback and energy loss at TOA.
38 Decreasing land albedo causes a northwards shift in the zonal mean intertrop-
39 ical convergence zone (ITCZ). The combined effects on ITCZ location of all
40 atmospheric feedbacks roughly cancel for the albedo forcing; the total ITCZ
41 shift is comparable to that predicted for the albedo forcing alone. For an im-
42 posed increase in evaporative resistance that reduces land evaporation, low
43 cloud cover decreases in the northern mid-latitudes and more energy is ab-
44 sorbed at TOA there; longwave loss due to warming provides a negative feed-
45 back on the TOA energy balance and ITCZ shift. Imposed changes in land
46 albedo and evaporative resistance modulate fundamentally different aspects
47 of the surface energy budget. However, the pattern of TOA radiation changes
48 due to the water vapour and air temperature responses are highly correlated
49 for these two forcings because both forcings lead to near-surface warming.

50 **1. Introduction**

51 Changes in land surface properties, such as those associated with changes in vegetation, modu-
52 late fluxes of energy and water between land and the overlying atmosphere (Charney et al. 1975;
53 Shukla and Mintz 1982; Koster et al. 2004, 2006; Davin et al. 2010; Laguë et al. 2019). Changes
54 in land surface properties can directly modify surface temperatures by re-partitioning surface en-
55 ergy fluxes between sensible and latent components (Lee et al. 2011; Devaraju et al. 2018; Laguë
56 et al. 2019). By modifying the overlying atmosphere, land surface changes can also indirectly al-
57 ter local surface climate by changing radiation and surface turbulent fluxes in ways that constitute
58 feedbacks on the original land surface perturbation (Betts et al. 1996). Furthermore, land-driven
59 atmospheric changes can lead to changes in terrestrial climate both in the region of the original
60 land surface change and in regions far removed from that initial change (Charney et al. 1975; Bo-
61 nan et al. 1992; Swann et al. 2012; Laguë and Swann 2016; Devaraju et al. 2018; Winckler et al.
62 2018; Laguë et al. 2019).

63 Changes in land surface properties modify climate by modulating the flux of energy between
64 land and the base of the atmosphere. Surface albedo directly influences the solar energy absorbed
65 by land, with darker land such as forests absorbing more sunlight than brighter land such as deserts
66 (Budyko 1961, 1969; Payne 1972; Bonan 2008, and references therein). The land surface has a
67 small heat capacity compared to the ocean and does not efficiently move energy laterally (Cess and
68 Goldenberg 1981; North et al. 1983; Milly and Shmakin 2002; Bonan 2008). Thus, over annual
69 timescales, changes in solar and longwave energy absorbed by land cause changes in longwave
70 radiation, sensible heat, and latent heat emitted by land; that is, the land surface energy budget is
71 closed over sufficiently long timescales such as the annual cycle (Manabe 1969; Budyko 1982).
72 Latent heat flux from land to the atmosphere is modulated not only by surface water availability

73 and atmospheric water vapor demand, but also by physical properties of the land surface (Budyko
74 1961, 1969). For example, vegetation can actively modify the flux of water from land to the
75 atmosphere by regulating transpiration through the opening and closing of stomata (leaf pores that
76 control gas exchange) (Sellers et al. 1996).

77 Changes in land surface albedo and evaporation have been demonstrated to be capable of driving
78 large-scale shifts in atmospheric circulation (Charney et al. 1977; Shukla and Mintz 1982). Davin
79 et al. (2010) explored the effects of albedo, evaporation, and roughness of a completely forested
80 vs. grass-covered world, while Swann et al. (2012) demonstrated how mid-latitude forest cover can
81 shift the location of the Intertropical Convergence Zone (ITCZ) in a global climate model. Such
82 changes in global circulation can be understood, in part, using the vertically integrated atmospheric
83 energy budget. For example, changes in surface ice cover, vegetation, or idealized energy sources
84 have been shown to modify large-scale atmospheric circulation and tropical precipitation, with the
85 zonal mean location of the ITCZ shifting towards the energy-rich hemisphere (Chiang and Bitz
86 2005; Broccoli et al. 2006) or, more precisely, toward the hemisphere containing the anomalous
87 positive energy source (Kang et al. 2008, 2009; Swann et al. 2012; Laguë and Swann 2016; Kang
88 2020; Geen et al. 2020).

89 To understand the atmospheric response to an imposed change in the climate system, it can be
90 useful to decompose the response into that produced directly by the forcing and that arising from
91 individual feedbacks. For example, increased atmospheric carbon dioxide concentrations directly
92 affect longwave radiation (the forcing) and initiate feedbacks by other aspects of the climate sys-
93 tem (e.g. changes in cloud cover or sea ice extent) which further modify shortwave (SW) and
94 longwave (LW) radiation at both the top of the atmosphere (TOA) and the surface (Andrews et al.
95 2012). For low-latitude rainfall changes, these feedbacks can be large compared to the forcing
96 (Kang et al. 2009; Cvijanovic and Chiang 2013), making it difficult to understand and predict how

97 an imposed land surface change which modifies the atmospheric energy budget will alter local and
98 remote surface climate.

99 In this study, we investigate how idealized changes in land surface properties modify large-
100 scale atmospheric circulation and precipitation, both through their direct effect on fluxes of energy
101 into the atmosphere and through radiative feedbacks. We first use climate model simulations
102 to study how global-scale changes in land surface albedo and evaporative resistance modify the
103 atmospheric energy source (i.e. the net flux of energy into the atmosphere through its top and
104 bottom boundaries). While many more studies have focused on the influence of land surface albedo
105 on climate (e.g. Charney et al. 1977; Dickinson 1983; Broccoli and Manabe 1987), evaporative
106 resistance is also important (e.g. Shukla and Mintz 1982; Sellers et al. 1996; Laguë et al. 2019;
107 Zarakas et al. 2020). Evaporative resistance controls the surface latent heat flux for a given vapor
108 pressure deficit of surface air, and is a bulk proxy for many surface and vegetative processes that
109 control water vapor flux.

110 We attribute changes in the atmospheric energy source to the direct effect of the imposed land
111 surface change (in albedo or evaporative resistance) and to feedbacks resulting from (i) albedo
112 changes due to snow and ice cover, (ii) changes in atmospheric water vapour, (iii) changes in
113 temperatures, and (iv) changes in cloud cover. Each of these components of the change in the
114 atmospheric energy source can, through the vertically integrated atmospheric energy budget, be
115 directly associated with a change in atmospheric energy transport. Since, in Earth's tropics, both
116 precipitation and atmospheric energy transport are primarily accomplished by time-mean overturn-
117 ing circulations, this allows us to attribute changes in tropical circulation and tropical precipitation
118 to the imposed land surface forcing and the feedbacks.

119 **2. Methods**

120 *a. Model*

121 We use a modified version of the Community Earth System Model (CESM) (Hurrell et al. 2013),
122 consisting of the Community Atmosphere Model v. 5 (CAM5) coupled to a slab ocean model, the
123 CICE5 interactive sea ice model (Bailey et al. 2018), and a simplified land model. The slab
124 ocean allows sea surface temperatures (SSTs) to change but uses prescribed ocean heat transport
125 (Neale et al. 2012); this allows atmospheric circulation more freedom to change over both land and
126 oceans than in a fixed-SST simulation. The prescribed ocean heat transport is identical across all
127 simulations. Instead of the Community Land Model (CLM) (Oleson et al. 2013; Lawrence et al.
128 2019), we use the Simple Land Interface Model (SLIM) (Laguë et al. 2019), which allows us to
129 explicitly control individual land surface properties in a way that is not possible with more complex
130 land surface models such as CLM. Simulations are run at roughly 2° horizontal resolution.

131 *b. Simulations*

132 Two land surface properties are perturbed for this study: albedo and evaporative resistance.
133 Albedo is a measure of the fraction of incident shortwave radiation that the land surface reflects,
134 while evaporative resistance modifies the difficulty of evaporating water from land. In the context
135 of vegetation, albedo is modulated by leaf color, leaf angle, and leaf area; evaporative resistance
136 is a combined result of soil moisture, root depth, leaf area, and stomatal conductance. In SLIM,
137 both surface properties are directly controlled by the user.

138 We modify the prescribed, snow-free albedo of the land surface for visible shortwave radiation
139 (both direct and diffuse streams). A portion of the total modelled shortwave radiation incident
140 upon the land surface occurs in the near-infrared (near-IR), but we hold the snow-free land surface

141 albedo in the near-IR fixed across all simulations. We only modify the land surface albedo over
142 non-glaciated regions. The total land surface albedo can be modified by the presence of snow,
143 which masks the bare-ground albedo and results in a brighter surface; as such, the actual change
144 in albedo that affects radiation is smaller than the snow-free albedo change imposed on the land
145 surface.

146 The evaporative resistance that we modify in SLIM modulates the difficulty of evaporating water
147 from land. The hydrology in SLIM is represented by a bucket at each land point. To evaporate
148 water from the bucket, there is a combined resistance due in part to how full the bucket is (analo-
149 gous to soil moisture), and in part to the imposed evaporative resistance at each point (analogous
150 to properties such as vegetation root depth or stomatal conductance). It is this second resistance
151 term which we modify in our simulations; the soil moisture is free to evolve.

152 Three primary simulations are used in this study, while two additional simulations are leveraged
153 to calculate the relationship between ITCZ latitude and cross-equatorial atmospheric energy trans-
154 port. Each simulation is run for a total of 50 years, with the first 20 years discarded to allow the
155 model time to spin up. Note that the model simulations used in this study are a subset of the same
156 simulations used in Laguë et al. (2019).

157 The first “baseline” simulation uses moderate values for land surface albedo ($\alpha = 0.2$) and
158 evaporative resistance ($r_s = 100$ s/m). The second simulation explores the effect of making land
159 darker ($\alpha = 0.1$, $r_s = 100$ s/m), while the third explores the effect of making it harder to evaporate
160 water from land ($\alpha = 0.2$, $r_s = 200$ s/m). An albedo of 0.2 is roughly comparable to that of a
161 grassland, while an albedo of 0.1 is comparable to that of a forest (see Bonan 2008, and references
162 therein). A change in evaporative resistance from 200 to 100 s/m is comparable to a change in
163 the canopy-level stomatal conductance between needleleaf and broadleaf forests (Bonan 2016).
164 Two additional simulations from Laguë et al. (2019)—one with a land surface albedo of 0.3,

165 which is comparable to that of a desert, and the other with an evaporative resistance of 30 s/m,
166 which is comparable to that of a well-watered crop—are used to calculate the relationship between
167 annual mean cross-equatorial atmospheric energy transport AET_{eq} and annual mean ITCZ latitude
168 as measured by the center of mass of tropical precipitation, ϕ_p (see appendix for calculations of
169 AET_{eq} and ϕ_p). These simulations each provide an additional 30 years of spun-up data for our
170 linear fit of ΔAET_{eq} vs. $\Delta\phi_p$.

171 All other land surface properties are identical across simulations, and across space. That is,
172 all simulations have the same spatially uniform values for aerodynamic roughness (0.1 m), the
173 capacity of land to hold water (200 mm), soil thermal properties, etc. Glaciated land points have
174 thermal and radiative properties consistent with ice (Laguë et al. 2019).

175 *c. Approach*

176 Here, we outline the general approach used in this study. Details on specific calculations are
177 provided in the Appendix. We modify each of the two land surface properties (albedo and evap-
178 orative resistance) in isolation. Each change in land surface property drives a change in net TOA
179 radiation (TOA_{net}), a change in zonal mean cross-equatorial atmospheric heat transport, and a shift
180 in the zonal mean location of the ITCZ.

181 Using a combination of model output and radiative kernels for albedo, temperature, and water
182 vapour, we decompose the total change in TOA radiation into the change in TOA *SW* directly due
183 to the imposed change in land surface albedo, the change in TOA *SW* due to changes in albedo
184 from changes in snow/ice cover, the change in TOA *LW* due to changes in surface temperature
185 and atmospheric temperatures, the changes in TOA *SW* and *LW* due to changes in column water
186 vapour, and the changes in TOA *SW* and *LW* due to changes in cloud cover.

187 We meridionally integrate TOA_{net} , under the assumption that atmospheric energy storage is
188 negligible on annual time scales, to calculate cross-equatorial atmospheric energy transport AET_{eq} ,
189 and estimate the linear relationship between AET_{eq} and the zonal-mean location of the ITCZ.
190 We measure the zonal-mean ITCZ location as the latitude ϕ_p that is the center of mass of the
191 precipitation distribution between 20°S-20°N. Using the individual contribution to ΔTOA_{net} from
192 each surface or atmospheric process resulting from the imposed change in land surface property
193 (e.g. the change in albedo from changes in snow/ice, or the change in water vapour), we determine
194 the ΔAET_{eq} that would result from that individual component of the TOA_{net} response alone. We
195 then leverage the derived relationship between AET_{eq} and ϕ_p to attribute portions of the total
196 modelled shift in the ITCZ to each individual atmospheric and surface process. The practice of
197 meridionally integrating anomalous TOA energy sources to obtain an AET_{eq} change and then an
198 ITCZ shift follows Kang et al. (2008), and using this procedure to estimate radiative feedbacks
199 follows Peterson and Boos (2020).

200 We follow the methodology of Soden et al. (2008) and Pendergrass et al. (2018) to decompose
201 the response of TOA radiation into components associated with changes in imposed land surface
202 albedo, changes in albedo due to changes in snow and ice, changes in water vapor, changes in
203 surface and air temperatures, and changes in cloud cover. Details of the calculations used in this
204 study are provided in the Appendix.

205 **3. Results**

206 Decreasing land surface albedo and increasing land surface evaporative resistance both gen-
207 erate changes in the TOA energy balance with distinct spatial and seasonal patterns (figure 1).
208 Decreasing land surface albedo results in more energy absorbed at the TOA over most land re-
209 gions, particularly during local summer when insolation is high, while increasing land surface

210 evaporative resistance modifies the TOA energy budget mostly in the northern mid-to-high lati-
211 tudes during boreal summer. Decreasing land albedo and increasing land evaporative resistance
212 both lead to overall more energy absorbed at the TOA over the Northern Hemisphere, though for
213 different reasons which are explored below.

214 The land albedo and evaporative resistance changes also produce changes in precipitation over
215 both land and ocean throughout the globe. Past studies have demonstrated that hemispheric im-
216 balances in atmospheric energy sources lead to shifts in the ITCZ towards the positive energy
217 source anomaly (e.g. Chiang and Bitz 2005; Broccoli et al. 2006; Kang et al. 2008; Swann et al.
218 2012; Laguë and Swann 2016; Kang 2020). In our simulations, changes in land surface albedo
219 and evaporative resistance both lead to northward shifts in the ITCZ (figure 2; the general pattern
220 of positive precipitation anomalies to the north of the equator and negative anomalies to the south
221 indicate a northward shift of the tropical precipitation maximum). Here, we investigate the mech-
222 anisms contributing to the change in the TOA energy budget, and quantify the association between
223 changes in the TOA radiative balance and changes in the atmospheric energy transport and zonal
224 mean tropical precipitation. We focus these analyses on the annual mean.

225 *a. Decreasing Land Surface Albedo*

226 The spatially uniform decrease in snow-free land albedo has a spatially non-uniform impact
227 on TOA_{net} . Darkening land results in more SW being absorbed by Earth over most land areas,
228 while over oceans and parts of the northern high-latitudes, more energy is lost by the Earth system
229 (figure 1a). The peak anomalous energy gain resulting from the decreased land albedo is found in
230 the tropics in the annual mean, with smaller increases in the mid-latitudes.

231 To understand the mechanisms through which a spatially uniform change in land surface albedo
232 causes a spatially non-homogeneous and non-local change in TOA radiation, we decompose the

233 response into a forcing and several feedbacks, each of which impact the TOA flux of shortwave
234 (*SW*) or longwave (*LW*) radiation. For our analysis of changes in TOA energy fluxes, all fluxes
235 (*SW* and *LW*) are defined to be positive *downwards* such that positive anomalies indicate more
236 energy into the Earth system.

237 1) ALBEDO FORCING

238 The imposed decrease in land surface albedo directly forces an increase in absorbed solar radia-
239 tion at the surface, and in turn reduces the amount of *SW* leaving the atmosphere at the TOA. Using
240 the all-sky (i.e. including the effects of clouds) radiative kernel for albedo for CAM5 (Pendergrass
241 et al. 2018), we calculate how our imposed change in land surface albedo directly modifies TOA
242 *SW* assuming temperatures, water vapour, snow and ice cover, and cloud cover do not change.
243 The imposed decrease in land surface albedo causes an increase in net TOA *SW* radiation over all
244 non-glaciated land areas (that is, everywhere the albedo was directly changed; figure 3a). Within
245 snow-free land regions, the spatial pattern in the change in TOA *SW* radiation comes predomi-
246 nantly from the spatial pattern of the radiative kernel itself, which reflects the pattern of insolation,
247 cloudiness, and clear-sky optical depth (figure S1). From the kernel, we see that the increase in
248 absorbed TOA *SW* for a spatially uniform decrease in land albedo is largest in low latitudes, where
249 incident solar radiation is highest and the annual mean atmospheric path length for downwelling
250 shortwave is smallest. The same albedo change imposed on regions with climatologically high
251 cloud cover (e.g. the Maritime Continent) has a smaller impact on TOA *SW* than regions at a
252 similar latitude with less cloud cover, as less *SW* reaches the surface in those regions. The direct
253 forcing of the imposed albedo change is calculated here specifically for snow-free albedo, i.e. how
254 the TOA *SW* would be affected in the absence of snow. However, land surface albedo in higher

255 latitudes is masked by snow for part of the year; the change in TOA radiation because of changes
256 in snow and ice is captured in the albedo feedback term discussed next.

257 2) ALBEDO FEEDBACK

258 We define albedo feedbacks as changes in TOA *SW* radiation due to changes in snow and ice
259 cover, which themselves result from changes to the climate system *driven* by our imposed change
260 in land surface property. Decreasing land surface albedo leads to warming near the land surface
261 (see Laguë et al. 2019), causing sea ice loss and changes in snow cover in the high latitudes
262 (supplemental figures S2, S3). Using the radiative kernel for albedo, we can quantify the effect of
263 albedo changes resulting from changes in snow and ice on TOA *SW*. The albedo feedback on the
264 imposed decrease in snow-free land albedo is positive (i.e. more *SW* absorbed at the TOA) over
265 regions of snow and sea ice loss, with most of the changes occurring in the northern high latitudes
266 (with some loss of sea ice along the ice edge of Antarctica; figure 3b).

267 3) WATER VAPOUR FEEDBACKS

268 Decreased land surface albedo can modify atmospheric water vapour both by modulating evapo-
269 ration from the land surface and by modulating the winds that transport water vapour. Decreasing
270 land albedo leads to more water vapour over tropical land in our model, with atmospheric tem-
271 peratures and specific humidities both generally increasing over land. There is also a meridional
272 dipole pattern in precipitable water over tropical oceans reflecting a northwards shift in the ITCZ
273 and a change in the humidity of the subtropical dry zones (figure S4). In idealized aquaplanet
274 models, the relative humidity of the subtropical dry zones increases in the hemisphere in which a
275 positive energy source is imposed and decreases in the subtropical dry zones on the other side of
276 the equator, amplifying the more traditional fixed-relative humidity water vapor feedback (Peter-

son and Boos 2020); this also seems to occur in our model in response to land albedo changes. The only statistically significant changes in *SW* at the TOA due to water vapour changes in response to decrease land albedo occur over the Sahara and Arabian Peninsula, where the response is positive (i.e. more *SW* absorbed by the enhanced water content; figure 3c). The *LW* effects of water vapour changes are also positive, but are much more far reaching, spreading over most land and ocean regions of the NH (figure 3d). Averaged globally, the *LW* effects of changes in atmospheric water vapour are as large as the direct effect of both the albedo forcing and ice-albedo feedback on TOA *SW*, with both contributing an extra 2 W/m^2 of energy to the Earth system at the TOA (table 1).

4) TEMPERATURE FEEDBACKS

Temperature feedbacks are changes in TOA *LW* due to changes in surface temperature, T_s , and temperatures through the atmospheric column. These combine the Planck and lapse rate feedbacks, with the latter typically having a magnitude that is about one-third that of the former in the global mean (Soden and Held 2006). Using the radiative kernel for temperature, we see that temperature feedbacks produce an increase in outgoing *LW* that opposes the *SW* forcing, as expected for negative feedbacks. Changes in T_s drive an increase in outgoing *LW* mostly over NH land and the Arctic ocean (figure S5). In contrast, changes in atmospheric temperatures result in more outgoing *LW* over most land and ocean regions, due to large-scale atmospheric warming as a result of decreasing land albedo (figure 3e). Changes in TOA *LW* in response to decreased land albedo provide the strongest globally averaged change in the TOA energy budget, yielding a global average of 2.8 W/m^2 of energy loss at the TOA (table 1). This is expected for the negative Planck and lapse rate feedbacks, which balance the sum of the forcing and the positive water vapor and albedo feedbacks to achieve TOA energy balance in the new steady state.

299 5) CLOUD FEEDBACKS

300 Cloud feedbacks are changes to net TOA *SW* and *LW* as a result of changes in cloud cover.
301 Changes in cloud radiative forcing that occur in the absence of any changes in cloud cover are
302 not included in this definition of cloud feedbacks, as detailed in the Appendix and discussed by
303 Soden et al. (2008). We consider cloud feedbacks to be positive if the change in cloud cover leads
304 to an increase in net energy absorbed at the TOA. Globally, the combined *SW* and *LW* effect of
305 changes in cloud cover in response to decrease land albedo is a net loss of energy from the Earth
306 system (figure 3f). Over most land regions, a decrease in land albedo results in an increase in cloud
307 cover that accompanies the precipitation increase (e.g. figure 2a), producing greater reflection of
308 TOA *SW* (figure 3g) and enhanced *LW* trapping over land (figure 3h). Some reductions in cloud
309 cover occur over ocean, with reduced *SW* reflection and reduced *LW* trapping by clouds being
310 especially prominent where reduced rainfall south of the equator accompanies the northward shift
311 of the ITCZ (cf. figures 2a and 3g, h). The *SW* and *LW* effects of cloud changes nearly cancel in
312 regions where high cloud changes accompany ITCZ shifts, while the *SW* effects of cloud changes
313 dominate in regions where low clouds change (e.g. the upwelling zones in eastern ocean basins).
314 However, in the global mean the effects of cloud changes are negative in both the *LW* and *SW*,
315 which contribute roughly equally to the global mean cloud feedback (table 1).

316 *b. Increasing Land Surface Evaporative Resistance*

317 Unlike decreasing land albedo, which causes more *SW* energy to be absorbed by land, chang-
318 ing the evaporative resistance of land does not directly modify the total energy absorbed by land.
319 Increasing evaporative resistance drives a repartitioning of surface energy fluxes, where energy
320 previously used to evaporate water is instead partitioned into sensible heat flux or emitted long-
321 wave radiation, both of which result from the increase in surface temperature that is driven by the

322 reduced evaporative cooling. Changes in evaporative resistance can only modify latent heat flux
323 from the surface to the atmosphere in regions where there is water stored on the land surface; there
324 is little to no effect of changing this surface property over desert regions.

325 Here we discuss the net response to the evaporative resistance forcing, and briefly summarize all
326 of the individual components of that response. In contrast to the response of TOA_{net} to decreasing
327 land albedo, increasing the evaporative resistance of land results in an increase in TOA_{net} that
328 is strongest in the northern mid-latitudes during June-August (figure 1b, d). As stated above,
329 changing the evaporative resistance of land has no *direct* impact on the total energy absorbed by
330 land, so there is no “forcing” in the context used for the albedo simulations. However, we can still
331 decompose changes in the TOA energy budget into components due to snow/ice changes, water
332 vapour, temperatures, and clouds.

333 Increasing the evaporative resistance of land leads to warming by suppressing latent cooling
334 of the land surface, which causes a reduction of snow and sea-ice (figure S3). This reduces the
335 surface albedo and leads to an increase in absorbed SW at the TOA, mostly in the northern high
336 latitudes during boreal summer (figure 1d, 4b; note the change in color scale in figure 4). There are
337 no statistically significant changes in TOA SW due to changes in atmospheric water vapour, while
338 the LW effects of water vapour changes lead to a slight increase in energy absorbed by Earth at
339 the TOA over parts of the low latitude ocean (figure 4c, d). We note that total column water vapor
340 actually increases over most of the Northern Hemisphere, which has the largest land area (figure
341 4b). That is, increased land resistance leads to decreased land evaporation and less low cloud
342 cover, which drives warming which itself results in more atmospheric water vapor, particularly
343 over the oceans, resulting from suppressed terrestrial evaporation. Increased surface temperatures
344 in the Arctic lead to more TOA LW loss, while atmospheric warming in the northern mid- to
345 high-latitudes also increases TOA LW loss (figure 4e).

346 The largest change to TOA radiation as a result of increasing the evaporative resistance of land
347 comes from the *SW* effects of changes in cloud cover (figure 4f,g). Loss of cloud cover over
348 southeastern North America and western Eurasia results in an increase in *SW* absorption by Earth.
349 This signal is strongest during NH summer, but persists with weaker magnitude over southeastern
350 North America during NH winter (figure 1d,f). Averaged globally, the *SW* and *LW* effects of cloud
351 cover changes on TOA_{net} , resulting from increased land surface evaporative resistance, largely
352 cancel (table 1).

353 *c. Cloud Forcing vs. Feedback*

354 In the previous two sections we quantified the cloud feedback, which results from a change in
355 cloud cover and is distinct from a change in the net radiative effects of clouds (which, in turn,
356 is often referred to as the cloud forcing; Soden et al. 2008). This distinction is important for
357 our imposed change in land surface albedo because the surface albedo change modifies the effect
358 of a fixed cloud distribution on the TOA *SW* flux, thus driving a change in *SW* cloud forcing
359 independent of any change in cloud cover. That is, changes in *SW* cloud forcing (figure S6). occur
360 both because of changes in cloud cover (the *SW* cloud feedback described above) and because of
361 changes in surface *SW* fluxes driven by the change in albedo independent of any changes in cloud
362 cover. The global mean *SW* cloud forcing is more than twice as large as the global mean cloud
363 feedback for the albedo forcing (-1.2 W/m² vs -0.5 W/m²). However, the *SW* cloud forcing and
364 *SW* cloud feedback are very similar for an increase in land evaporative resistance, because in that
365 case nearly all of the change in *SW* cloud forcing comes directly from a change in cloud cover.
366 The same physical process is thus captured by the *SW* cloud feedback and *SW* cloud forcing for
367 changes in evaporative resistance (figure S7).

368 *d. Pattern Correlation*

369 The pattern of the total TOA radiative response to a change in albedo or evaporative resistance
370 differs substantially (compare figure 1 a/b), with the two having a pattern correlation coefficient
371 of only 0.3 (table 2). However, for particular components of the TOA energy budget decompo-
372 sition explored above, the pattern is very similar for both forcings. Despite the two land surface
373 properties modifying fundamentally different aspects of the surface energy budget, the pattern of
374 the TOA response due to changes in water vapour, surface temperature, and air temperature are
375 similar for changes in albedo and evaporative resistance (compare individual panels of figure 3
376 to those in 4). Indeed, the pattern of the TOA response due to changes in water vapour, surface
377 temperature, and air temperature are strongly correlated for a change in land surface albedo and
378 land surface evaporative resistance (pattern correlation coefficients range from 0.7 to 0.9; table
379 2). This is because both the water vapour and temperature components of the TOA energy budget
380 decomposition are directly related to warming, and both decreasing the land surface albedo and
381 increasing land surface evaporative resistance lead to large-scale warming of the Earth system.
382 The mechanisms responsible for the surface warming are different; in the case of albedo, warming
383 is the direct result of increased *SW* absorption at the surface, while in the case of evaporative re-
384 sistance warming is the result of suppressed evaporative cooling and increased *SW* absorption due
385 to regional loss of cloud cover. However, in both cases, warming at the surface is accompanied by
386 warming aloft and an increase in atmospheric water vapour over large parts of the northern hemi-
387 sphere remote from the forcings (figure S8), presumably due to homogenization of atmospheric
388 temperature and moisture by basic state winds.

389 *e. Attribution of Zonal Mean ITCZ Shift*

390 In response to both decreased land surface albedo and increased land surface evaporative resis-
391 tance, there is a northwards shift in the ITCZ (figure 2a,b). Previous studies identified a strong
392 linear relationship between hemispheric energy imbalances, cross-equatorial atmospheric energy
393 transport, and the location of the ITCZ, both in models and in observations (Donohoe et al. 2013),
394 with the ITCZ shifting towards the hemisphere with the positive anomaly of net energy input
395 (Chiang and Bitz 2005; Kang et al. 2008; Swann et al. 2012; Laguë and Swann 2016; Kang 2020).

396 When land albedo is decreased, the Northern Hemisphere becomes the site of an anomalously
397 positive energy source as a result of increased absorption of *SW* by the larger land area in the
398 Northern Hemisphere. When land evaporative resistance is increased, loss of low cloud cover
399 in the northern mid-latitudes allows more sunlight to reach the surface over portions of northern
400 mid-latitude land, also resulting in an anomalously positive energy source in the Northern Hemi-
401 sphere. In both cases, the vertically integrated atmospheric energy budget balanced by a time-
402 mean decrease in atmospheric energy transport from the Southern Hemisphere into the Northern
403 Hemisphere, and a corresponding northwards shift in the zonal mean location of the ITCZ (figure
404 2).

405 The relationship between annual mean cross-equatorial atmospheric energy transport and the
406 zonal mean ITCZ latitude ϕ_p is strongly linear in our simulations (figure 5). We find a -4.4° shift
407 in the ITCZ per 1 PW increase in annual mean northwards cross-equatorial atmospheric energy
408 transport (figure 5). This slope is slightly larger in magnitude than that found by Donohoe et al.
409 (2013) across CMIP5 models ($-2.4^\circ/\text{PW}$) and from observations of the seasonal cycle in present-
410 day climate ($-2.7^\circ/\text{PW}$).

411 The relationship between the zonal mean ITCZ location, ϕ_p , and cross-equatorial atmospheric
412 energy transport, AET_{eq} , in response to perturbed land surface properties is also tightly correlated
413 during Northern Hemisphere summer (figure 5a, c). However, we wish to decompose the ITCZ
414 shift into components associated with individual feedbacks (e.g. water vapor and Planck feed-
415 backs), which requires meridionally integrating the anomalous TOA energy flux due to each feed-
416 back to obtain its contribution to the net cross-equatorial energy transport (e.g. Kang et al. 2008;
417 Peterson and Boos 2020); this can only be done exactly in the annual mean, when the transient
418 atmospheric storage term is zero in a steady state climate. In order to leverage our decomposition
419 of the TOA energy budget, we thus focus our analysis of shifts in the ITCZ on the annual mean.

420 For each component of the TOA energy budget response to changes in land surface albedo and
421 evaporative resistance, we calculate the anomalous cross-equatorial energy flux needed to bal-
422 ance the specific pattern and magnitude of TOA *SW* and *LW* change comprising that component.
423 Then, using the linear relationship between cross-equatorial energy transport and ϕ_p , we quantify
424 how much of a shift in the ITCZ we would expect from each individual component of the TOA
425 energy budget response (figure S9 provides a heuristic illustration). Reducing albedo and increas-
426 ing evaporative resistance both drive northward shifts in cross-equatorial energy transport and the
427 ITCZ (figure 6, dark grey bars), but the processes responsible for these changes differ for the two
428 surface forcings. Since our primary interest is in the relative magnitudes of different feedbacks on
429 a given forcing, we rescale the net ITCZ shift produced by each imposed change in land surface
430 property so that it has a value of $+1^\circ$ (figure 6, dark gray bars).

431 Decreasing land albedo drives a northwards shift in the ITCZ as a result of the direct effect of
432 the imposed change in albedo, with positive (northward) contributions from the albedo feedback
433 due to changes in snow and ice, the *SW* and *LW* water vapour feedbacks, and the *LW* cloud
434 feedback (figure 6). It is notable that the *LW* cloud effects provide a negative feedback on the

435 global mean TOA energy balance response to the albedo forcing (Table 1) but a positive feedback
436 on the ITCZ response; this is the result of the specific pattern of the *LW* cloud feedback. Changes
437 in surface temperature, air temperature, and the *SW* effects of cloud cover changes all act as
438 negative feedbacks that reduce the northward shift of the ITCZ. Of all the feedbacks on the albedo
439 forcing, the Planck feedback is largest, consistent with global mean feedbacks on the CO₂ forcing
440 of global mean temperature; water vapor feedbacks are about an order of magnitude larger than
441 the net cloud feedback. The cloud feedbacks seem to be dominated by tropical cloud changes
442 (figure 3f,g,h) and exhibit strong cancellation between *SW* and *LW* components. The effect of all
443 of the feedbacks on the imposed change in land surface albedo largely cancel, such that the actual
444 modelled shift in the ITCZ is comparable to the shift in the ITCZ that would be realized by the *SW*
445 effects of the imposed change in land surface albedo alone. A similar cancellation of all feedbacks
446 was seen in the one-dimensional energy balance model of Peterson and Boos (2020), although that
447 model used an entirely oceanic lower boundary and did not examine land surface forcings.

448 Increasing the evaporative resistance of land reduces terrestrial evaporation and leads to warm-
449 ing. There is no directly imposed change in TOA radiation that can be viewed as an imposed
450 forcing, but we are nevertheless able to quantify the contribution of each feedback to the total
451 ITCZ shift. The dominant positive contributors to the northwards shift of the ITCZ in response
452 to increased evaporative resistance are the change in TOA *SW* due to changes in cloud cover and
453 the change in TOA *LW* due to changes in water vapor. The water vapor-induced *LW* changes are
454 interesting because they result primarily from increases in humidity over the low-latitude oceans,
455 contrasting with the reduction in land humidity expected to result from an increase in land evapo-
456 rative resistance. The component that comes closest to constituting a forcing, from the perspective
457 of the energy budget, is the loss of low cloud cover in the northern midlatitudes, which results in a
458 hemispheric energy imbalance with more energy being added to the NH than the SH in response

459 to decreased land evaporation. Unlike in the case of albedo, the *LW* effects of changes in cloud
460 cover act in the same direction as the *SW* effects, although the *LW* cloud contribution is relatively
461 small. While changes in tropical clouds dominate the cloud feedbacks in response to a change
462 in land albedo, extra-tropical clouds dominate the cloud feedback in response to changes in land
463 evaporative resistance, with *SW* cloud effects greatly exceeding any cancellation from *LW* cloud
464 effects. Changes in TOA *SW* due to changes in cloud cover alone would result in a roughly 1.6°
465 northwards shift in the ITCZ, and the *LW* effect of changes in water vapor would drive an addi-
466 tioanl 1.7° northwards shift, but this northwards shift is damped by a strong 3.0° southward shift
467 resulting from *LW* feedbacks driven by combined surface and atmospheric warming. While there
468 is a contribution to a northward ITCZ shift from loss of high-latitude snow and ice resulting from
469 warming, this contribution is smaller than the contributions from temperatures, water vapour, and
470 *SW* cloud feedbacks, and is not statistically significant.

471 The ITCZ shift predicted by the sum of the feedbacks is larger than the modelled ITCZ shift,
472 more so for evaporative resistance than for albedo (light gray bars in figure 6). This disagreement
473 is the result of the linear fit used to predict the ITCZ shift associated with a given change in cross-
474 equatorial energy transport not perfectly intersecting the interannual mean of the three model
475 simulations (compare dashed line to large markers in figure 5a). However, we note that since
476 these are re-scaled values and the net zonal-mean, model-simulated ITCZ shift for the evaporative
477 resistance forcing is only about 0.3° in a model with a horizontal grid spacing of about 2° , this
478 non-linearity may be negligible compared to discretization and other numerical uncertainties.

479 **4. Summary and Discussion**

480 Both albedo and evaporative resistance of the land surface can drive large changes in the TOA
481 radiation balance. However, the pathways through which these land surface properties modify

482 the TOA radiative budget differ. This study provides a breakdown of the impact of individual
483 land surface property changes on TOA radiation, zonally averaged AET_{eq} , and zonal mean ITCZ
484 location. We leverage atmospheric radiative kernels to decompose the effect of decreasing land
485 surface albedo and increasing land surface evaporative resistance on the TOA energy balance.

486 Decreasing land surface albedo leads to an overall increase in energy absorbed at the TOA over
487 land regions, and a compensating increase in energy lost from the TOA over ocean regions. The
488 surface warming caused by the imposed reduction in surface albedo leads to reduced snow and
489 ice cover that, in turn, cause even more SW to be absorbed by the Earth system. The LW effects
490 of changes in atmospheric water vapor driven by the reduction in land surface albedo also lead to
491 an increase in energy absorbed at the TOA, while warming of surface and air temperatures and
492 changes in cloud cover lead to energy loss from the TOA.

493 Changes in land surface albedo are strongly attenuated by the atmosphere. That is, for a given
494 change in surface albedo, the change in planetary albedo (the fraction of insolation not absorbed by
495 the climate system) is much smaller (Donohoe and Battisti 2011). Nonetheless, we have demon-
496 strated that changes in land surface albedo can modify TOA net radiation not only directly by
497 modifying the net flux of SW radiation, but also indirectly by modifying atmospheric tempera-
498 tures, water vapor content, cloud cover, etc. Furthermore, land albedo changes can produce shifts
499 in atmospheric circulations and rainfall, even if their influence on global mean planetary albedo is
500 modest.

501 Increasing land surface evaporative resistance primarily impacts the TOA radiative budget over
502 northern mid-latitude land regions. The SW effect of changes in cloud cover is the most direct
503 effect of the imposed increase in evaporative resistance, presumably resulting from reductions in
504 cloud cover caused by reduced humidity in the region of the forcing. Planck and water vapor
505 feedbacks act on this forcing in a similar way as for the albedo forcing; these feedbacks are geo-

506 graphically remote and have patterns of TOA energy flux change that are highly correlated for the
507 two forcings.

508 We use the relationship between cross-equatorial energy transport, as diagnosed from TOA en-
509 ergy fluxes, and the zonal mean location of the ITCZ to attribute northward shifts in precipitation
510 to individual surface and atmospheric responses to imposed land surface changes. The combined
511 effect of all atmospheric feedbacks on an imposed change in land surface albedo largely cancel,
512 and the resulting northward shift in the ITCZ is the same shift you would expect from the *SW*
513 effects of the imposed change in albedo alone. For the imposed increase in evaporative resistance,
514 the *SW* effect of clouds, combined with albedo changes due to reduced snow and ice cover as
515 a result of warming, results in a net northward shift in the ITCZ. For the evaporative resistance
516 forcing, the *SW* effect of clouds on ITCZ location is in the opposite direction as the *SW* effect of
517 clouds for the albedo forcing.

518 The idealized nature of these simulations necessarily presents some limitations. The perturba-
519 tions made to land surface albedo and evaporative resistance were applied to all non-glaciated land
520 surfaces, and as such the hemispheric imbalance in response to these land surface perturbations is
521 largely a result of the hemispherically asymmetric distribution of the continents in their present-
522 day configuration; other patterns of land surface change would yield their own specific patterns
523 of TOA energy flux changes and individual forcing/feedback terms. The radiative kernel we use
524 to decompose the TOA energy budget response into its components was generated with the same
525 atmospheric model as we use in this study (CAM5). However, any differences in the mean state of
526 atmospheric temperatures, humidity, and cloud cover between the CLM-CAM5 simulation used
527 for the kernels and the baseline SLIM-CAM5 simulation used in this study could introduce errors
528 in the kernel-predicted change in TOA radiation. Furthermore, because we do not have an explicit
529 radiative kernel for cloud fraction, any residuals that may exist in our calculations are lumped in

530 with the impact of clouds on TOA SW and LW , by virtue of the methods we use to decompose
531 the TOA energy balance (see Appendix). However, we expect these residuals to be small for two
532 reasons: (a) the mean state of SLIM-CAM5 is similar to the mean state of CLM-CAM5 (Laguë
533 et al. 2019, see) and (b) the patterns of ΔSW_{cloud} and ΔLW_{cloud} strongly resemble the change in
534 cloud fraction in our simulations, supporting the idea that they indeed result from changes in cloud
535 cover. Another important caveat is that we use a single atmospheric model and a single radiative
536 kernel in this study. While the direct effect of surface albedo on TOA SW radiation under clear-sky
537 conditions is similar across radiative kernels from multiple models (Soden et al. 2008; Shell et al.
538 2008; Flanner et al. 2011; Pendergrass et al. 2018), the response of cloud cover to a perturbation
539 can vary widely across models (Stocker et al. 2013; Zelinka et al. 2017). Particularly for the evap-
540 orative resistance forcing, for which cloud changes are the dominant driver of changes in the TOA
541 radiative budget, other atmospheric models could generate different patterns of TOA SW and LW
542 response. Finally, we focused on changes in zonal mean tropical rainfall, and it is known that
543 zonal mean changes are not generally representative of regional precipitation change (Byrne and
544 O’Gorman 2015; Kooperman et al. 2018; Atwood et al. 2020); we leave a detailed exploration of
545 the zonally resolved response for separate work.

546 Despite these caveats, the method we present here allows us to understand the mechanisms
547 through which changes in the land surface drive changes in zonal mean atmospheric circulation and
548 tropical precipitation. Understanding these mechanisms is critical to understanding how changes
549 in the land surface—both historical and in the future—impact climate locally and globally.

550 **5. Data Availability**

551 The data presented in this paper will be archived on Dryad and the link added here upon accep-
552 tance of this manuscript. The source code for the models used in this study are publicly available

553 on github at https://escomp.github.io/CESM/release-cesm2/downloading_cesm.html
 554 for CESM, and <https://github.com/marysa/SimpleLand> for SLIM.

555 *Acknowledgments.* MML acknowledges postdoctoral funding support from the James S. Mc-
 556 Donnell Foundation Postdoctoral Fellowship in Dynamic and Multiscale Systems and NSERC
 557 Grant PGSD3-487470- 2016. MML and ALSS acknowledge support from NSF Grant 1553715
 558 to the University of Washington. WRB acknowledges support from the U.S. Department
 559 of Energy, Office of Science, Office of Biological and Environmental Research, Climate
 560 and Environmental Sciences Division, Regional and Global Model Analysis Program, under
 561 Award DE-SC0019367. We acknowledge high-performance computing support from Cheyenne
 562 (doi:10.5065/D6RX99HX) provided by NCAR’s Computational and Information Systems Lab-
 563 oratory, sponsored by the National Science Foundation. We acknowledge additional comput-
 564 ing resources from the National Energy Research Scientific Computing Center (NERSC), a U.S.
 565 Department of Energy Office of Science User Facility operated under Contract No. DE-AC02-
 566 05CH11231.

567 APPENDIX

568 *a. TOA Energy Budget*

569 Decreasing land surface albedo or increasing land surface evaporative resistance modifies the
 570 energy balance at the surface (SFC_{net}) and top of atmosphere (TOA_{net}) (equations A1-A2).

$$TOA_{net} = SW_{TOA}^{\downarrow} - SW_{TOA}^{\uparrow} - LW_{TOA}^{\uparrow} \quad (A1)$$

$$SFC_{net} = SW_{SFC}^{\downarrow} - SW_{SFC}^{\uparrow} + LW_{SFC}^{\downarrow} - LW_{SFC}^{\uparrow} \\ - SH_{SFC} - LH_{SFC} \quad (A2)$$

571 At the TOA, the energy balance is between incoming shortwave (*SW*) radiation, reflected *SW*
572 radiation, and outgoing longwave radiation (*LW*). At the surface, the balance is between the net
573 flux of *SW* and *LW* radiation, and the turbulent fluxes of sensible heat (*SH*) and latent heat (*LH*).
574 The sign convention in equations A1-A2 is such that $SFC_{net} > 0$ means more energy absorbed
575 by the surface (land or ocean). More energy is absorbed by the Earth system in regions with
576 $TOA_{net} > 0$, while more energy is lost by the Earth system in regions with $TOA_{net} < 0$. On land
577 over sufficiently long timescales (e.g. the annual mean, which we examine here), the surface
578 energy budget balances, such that $SFC_{net} = 0$. The slab ocean model used in these simulations has
579 the same prescribed heat transport across all simulations; $SFC_{net} > 0$ in regions where the ocean
580 takes up atmospheric energy, and $SFC_{net} < 0$ in regions where the ocean releases energy to the
581 atmosphere.

582 Independent of any atmospheric feedbacks, a decrease in land albedo results in more shortwave
583 energy absorbed at the land surface, with a corresponding increase in the upwards surface energy
584 fluxes. In contrast, an increase in land evaporative resistance does not directly change the total
585 amount of energy absorbed or emitted by the land surface; rather, increasing evaporative resistance
586 reduces evaporation (i.e. reduces the latent heat flux), while sensible heat and upwards longwave
587 radiation increase to balance the surface energy budget. However, atmospheric responses to land
588 surface changes can modify both the downward fluxes of *SW* and *LW* at the surface, and the
589 outgoing fluxes of *SW* and *LW* at the TOA.

590 *b. Atmospheric Energy Transport*

591 We can calculate changes in atmospheric energy transport at the equator using two separate
592 approaches. In the annual mean only, we use changes in TOA_{net} and SFC_{net} (equation A3)

593 (Lintner et al. 2004).

$$\begin{aligned}
 AET_{eq} &= \int_0^{2\pi} \int_{-\frac{\pi}{2}}^0 2\pi a^2 \cos \phi (TOA_{net} - SFC_{net}) d\phi d\lambda \\
 &= - \int_0^{2\pi} \int_0^{\frac{\pi}{2}} 2\pi a^2 \cos \phi (TOA_{net} - SFC_{net}) d\phi d\lambda
 \end{aligned}
 \tag{A3}$$

594 $AET_{eq} > 0$ means positive energy transport by the atmosphere from the Southern to Northern
 595 Hemisphere. Cross-equatorial atmospheric heat transport can also be calculated directly from the
 596 meridional transport of moist static energy within the atmosphere evaluated at the equator $\langle vh \rangle_0$
 597 (equation A4).

$$\langle vh \rangle_0 = \left(\frac{1}{g} \int_{sfc}^{TOA} vh \right) \Big|_{lat=0}
 \tag{A4}$$

$$h = c_p T + L_v Q + gZ
 \tag{A5}$$

598 where v is the meridional wind and h is the moist static energy. vh is calculated from the heat
 599 capacity of dry air c_p , the latent heat of vapourization L_v , the meridional atmospheric transport of
 600 heat vT , the meridional atmospheric transport of moisture vQ , and the meridional transport of po-
 601 tential energy vZ . In the annual mean, AET_{eq} calculated from the TOA energy budget is identical
 602 to $\langle vh \rangle_0$ calculated from vertically integrated atmospheric energy and winds. Both methods give
 603 a strongly linear relationship, with roughly 4.2 PW of southwards atmospheric energy transport
 604 (as calculated by $\langle vh \rangle_0$) corresponding to a 1° northwards shift in the ITCZ, and with roughly 4.4
 605 PW of southwards atmospheric energy transport (as calculated from the TOA energy budget) cor-
 606 responding to a 1° northwards shift in the ITCZ. However, at sub-annual timescales, heat storage
 607 within the surface and the atmosphere cause AET (implied from the TOA energy budget) to dif-
 608 fer substantially from $\langle vh \rangle$ (actual/explicitly calculated atmospheric energy transport). Thus, the
 609 relationship between AET_{eq} and ϕ_p is only valid at annual mean timescales, while the relationship
 610 between $\langle vh \rangle_0$ and ϕ_p is valid on seasonal timescales as well (figure 5). However, we focus on an-
 611 nual mean AET_{eq} in this study in order to make use of changes in TOA radiation driven by specific

612 atmospheric and surface processes. Each of the individual forcing and feedback terms explored in
613 this study modify the TOA energy imbalance. Using the contribution of each term to TOA_{net} , we
614 leverage equation A3 to quantify the contribution of each forcing and feedback to AET_{eq} .

615 *c. Radiative kernel calculations*

616 We use a radiative kernel to diagnose the change in TOA_{net} resulting from the imposed change
617 in surface albedo, the change in surface albedo resulting from changes in snow and ice, the change
618 in surface temperature, the change in the vertical profile of air temperatures, and the change in
619 the vertical profile of atmospheric water vapour (Soden et al. 2008; Pendergrass et al. 2018).
620 Specifically, we leverage the radiative kernel from Pendergrass et al. (2018), which uses the same
621 atmospheric model (CAM5) as this study.

622 The kernel K gives the change in surface and TOA net SW and/or LW radiation resulting from a
623 1% change in surface albedo, a 1K change in surface temperature T_s , a 1K change in air tempera-
624 ture T at every vertical model level, and a change in water vapour q at every vertical model level
625 equivalent to a 1K increase in air temperature while maintaining constant relative humidity. The
626 kernel provides calculations for both “full sky” and “clear sky” conditions. The full sky kernel
627 gives the change in radiative fluxes resulting from each perturbation assuming cloud cover does
628 not change (but still allowing for the effects of climatological cloud cover). The clear sky kernel
629 gives the change in radiative fluxes resulting from each perturbation assuming there are no clouds
630 present. For our calculations, we focus on (a) the full sky radiative kernel and (b) the response of
631 TOA (not surface) SW and LW fluxes.

632 We use the following notation when referring to calculations using the radiative kernel. The
633 change in net TOA SW as a result of a 1% change in surface albedo is given by K_α . The change
634 in net TOA LW resulting from a 1K increase in surface temperature is given by K_{T_s} . The change

635 in TOA LW resulting from a 1K increase in air temperature vertically through the atmosphere is
 636 given by K_T . The change in TOA SW and LW resulting from the imposed change in water vapour
 637 are given by $K_{q,SW}$ and $K_{q,LW}$, respectively.

638 We impose a change in snow-free albedo $\Delta\alpha_i$ on the land surface. Using $\Delta\alpha_i$, we can quantify
 639 the change in top of atmosphere SW radiation directly attributable to the imposed change in surface
 640 albedo ΔSW_{α_i} (equation A6), where $\Delta\alpha_i$ is multiplied by 100 to convert it to a percent value.

$$\Delta SW_{\alpha_i} = K_{\alpha} \times 100 \times \Delta\alpha_i \quad (\text{A6})$$

641 The total modeled change in albedo includes both our imposed snow-free change in albedo as
 642 well as albedo changes due to snow and ice responses. We can calculate the change in albedo due to
 643 snow and ice changes (α_s) by subtracting the imposed change in albedo α_i from the actual modeled
 644 change in albedo α_m (figure S2; see also supplemental section ??). The change in albedo resulting
 645 from changes in snow and ice α_s is then multiplied by the radiative kernel to get the change in net
 646 TOA SW radiation resulting from albedo changes from snow and ice, ΔSW_{α_s} (equation A7).

$$\Delta SW_{\alpha_s} = K_{\alpha} \times 100 \times \Delta\alpha_s \quad (\text{A7})$$

647 Changes in surface temperature impact net TOA LW radiation; we determine how the specific
 648 surface temperature response to each land surface property change impacts TOA LW (ΔLW_{T_s}) using
 649 the radiative kernel for surface temperature (equation A8).

$$\Delta LW_{T_s} = K_{T_s} \times \Delta T_s \quad (\text{A8})$$

650 Changes in air temperature throughout the atmospheric column modify both the upwards and
 651 downwards flux of LW radiation through the atmosphere. Here, we are specifically interested
 652 in how changes in air temperature throughout the atmospheric column modify LW at the TOA
 653 (ΔLW_T). We multiply the radiative kernel for temperature by the change in temperature, then sum

654 over the atmospheric column to get the total effect of the air temperature changes at all vertical
 655 levels on TOA LW (equation A9).

$$\Delta LW_{\Delta T} = \sum_{SFC}^{TOA} K_T \times \Delta T \quad (A9)$$

656 Changes in atmospheric water vapour q modulate both SW and LW radiation. As with changes
 657 in T , we are interested in the vertical sum of the effect of Δq on TOA SW and LW . The raw
 658 kernel for water vapour K_q gives the change in radiative fluxes for the change in q associated
 659 with a 1K temperature change at constant relative humidity, while our simulations provide us with
 660 a Δq . Thus, we follow the methodology presented by Pendergrass et al. (2018) to calculate an
 661 intermediate kernel $K_q^* = K_q / \frac{\delta q}{\Delta T}$, where δT is the modelled change in air temperature and δq is
 662 the change in specific humidity that would have resulted from ΔT given constant relative humidity.
 663 Then, we can use K_q^* to determine the change in TOA SW and LW attributable to the modelled
 664 change in specific humidity Δq (equations A10-A11).

$$\Delta SW_{\Delta q} = \sum_{SFC}^{TOA} K_{q,SW}^* \times \Delta q \quad (A10)$$

$$\Delta LW_{\Delta q} = \sum_{SFC}^{TOA} K_{q,LW}^* \times \Delta q \quad (A11)$$

665 *d. Clouds*

666 To determine the effect of changes in cloud cover on TOA_{net} , we do not use a radiative kernel
 667 for cloud cover. Rather, we determine how much the modelled change in cloud fraction impacts
 668 SW and LW at the TOA, by calculating the total modelled response of TOA_{net} then subtract the
 669 change in TOA_{net} due to the combined effects of albedo, temperature, and water vapour (equations

670 A12-A13).

$$\begin{aligned} \Delta SW_{cloud} = & \Delta SW_{model} - K_{\alpha} \times \Delta \alpha_i \\ & - K_{\alpha} \times \Delta \alpha_s - \sum_{sfc}^{toa} K_{q,SW} \times \Delta q \end{aligned} \quad (A12)$$

671

$$\begin{aligned} \Delta LW_{cloud} = & \Delta LW_{model} - K_{T_s} \times \Delta T_s \\ & - \sum_{sfc}^{toa} K_T \times \Delta T - \sum_{sfc}^{toa} K_{q,LW} \times \Delta q \end{aligned} \quad (A13)$$

672 Because we do not diagnose ΔLW_{cloud} or ΔSW_{cloud} directly from a cloud kernel, the ΔLW_{cloud} or
 673 ΔSW_{cloud} terms necessarily also include any potential residual terms associated with the kernel.
 674 That is, if the actual direct response of TOA SW to $\Delta \alpha_i$ in our simulations differs from the ΔSW_{α_i}
 675 predicted by K_{α} because, for example, the mean state of cloud cover in our SLIM-CAM5 sim-
 676 ulations differs substantially from the mean state of cloud cover in the CLM-CAM5 model, that
 677 difference would necessarily be included in the ΔSW_{cloud} and ΔLW_{cloud} terms here.

678 We also consider changes in the shortwave cloud forcing ($SWCF$) and longwave cloud forcing
 679 ($LWCF$). This is a different quantity than ΔSW_{cloud} and ΔLW_{cloud} (see, for example, figure 11 in
 680 Soden et al. 2008). ΔSW_{cloud} and ΔLW_{cloud} are the change in TOA SW and LW radiation due to
 681 the change in cloud cover resulting from our imposed land surface property change. In contrast,
 682 the $SWCF$ and $LWCF$ quantify the difference in TOA SW and LW radiation between cloudy (full
 683 sky) and cloud-free (clear sky) conditions (equation A14-A15).

$$SWCF = SW_{clearsky} - SW_{fullsky} \quad (A14)$$

$$LWCF = LW_{fullsky} - LW_{clearsky} \quad (A15)$$

684 Note the different order of the full sky and clear sky terms for $SWCF$ vs. $LWCF$. This is because
 685 TOA SW (LW) fluxes are, by convention, positive downwards (upwards). This definition of $SWCF$
 686 and $LWCF$ is such that positive values indicate more energy into the system as a result of cloud

687 cover. Over land, *SWCF* is usually negative because clouds reflect sunlight, while *LWCF* is usu-
688 ally positive because cloud tops tend to radiate at cooler temperatures than the ground below them.
689 The *change* in *SWCF* and *LWCF* as a result of changes in land surface properties can occur with-
690 out any change in cloud cover (e.g. changing land surface albedo modifies $SW_{clearsky}$ and thus
691 *SWCF*), but can also occur as a result of changes in cloud cover.

692 **References**

693 Andrews, T., J. M. Gregory, M. J. Webb, and K. E. Taylor, 2012: Forcing, feedbacks and climate
694 sensitivity in CMIP5 coupled atmosphere-ocean climate models. *Geophysical Research Letters*,
695 **39 (9)**, 1–7, doi:10.1029/2012GL051607.

696 Atwood, A. R., A. Donohoe, D. S. Battisti, X. Liu, and F. S. R. Pausata, 2020: Robust
697 longitudinally-variable responses of the ITCZ to a myriad of climate forcings. *Geophysical*
698 *Research Letters*, **47 (17)**, 1–13, doi:10.1029/2020GL088833.

699 Bailey, D., E. Hunke, A. DuVivier, B. Lipscomb, C. Bitz, M. Holland, B. Briegleb, and
700 J. Schramm, 2018: CESM CICE5 Users Guide. Tech. rep., 47 pp. URL [https://buildmedia.
701 readthedocs.org/media/pdf/cesmcice/latest/cesmcice.pdf](https://buildmedia.readthedocs.org/media/pdf/cesmcice/latest/cesmcice.pdf).

702 Betts, A. K., J. H. Ball, A. C. Beljaars, M. J. Miller, and P. A. Viterbo, 1996: The land surface-
703 atmosphere interaction: A review based on observational and global modeling perspectives.
704 *Journal of Geophysical Research Atmospheres*, **101 (D3)**, 7209–7225, doi:10.1029/95JD02135.

705 Bonan, G., 2016: *Ecological Climatology*. 3rd ed., Cambridge University Press, doi:10.1017/
706 cbo9781107339200.

707 Bonan, G. B., 2008: *Ecological Climatology*. Cambridge Univ. Press, Cambridge, UK.

708 Bonan, G. B., D. Pollard, and S. L. Thompson, 1992: Effects of boreal forest vegetation on global
709 climate. *Nature*, **359 (6397)**, 716–718, doi:Doi10.1038/359716a0.

710 Broccoli, A. J., K. a. Dahl, and R. J. Stouffer, 2006: Response of the ITCZ to Northern Hemisphere
711 cooling. *Geophysical Research Letters*, **33 (1)**, 1–4, doi:10.1029/2005GL024546.

712 Broccoli, A. J., and S. Manabe, 1987: The influence of continental ice, atmospheric CO₂, and
713 land albedo on the climate of the last glacial maximum. *Climate Dynamics*, **1 (2)**, 87–99, doi:
714 10.1007/BF01054478.

715 Budyko, M. I., 1961: The Heat Balance of the Earth's Surface. *Soviet Geography*, **2 (4)**, 3–13,
716 doi:10.1080/00385417.1961.10770761.

717 Budyko, M. I., 1969: The effect of solar radiation variations on the climate of the Earth. *Tellus*,
718 **21 (5)**, 611–619, doi:10.3402/tellusa.v21i5.10109.

719 Budyko, M. I., 1982: The Earth's climate: past and future. *The Earth's climate: past and future.*,
720 doi:10.1016/0004-6981(83)90167-1.

721 Byrne, M. P., and P. A. O'Gorman, 2015: The response of precipitation minus evapotranspiration
722 to climate warming: Why the "Wet-get-wetter, dry-get-drier" scaling does not hold over land.
723 *Journal of Climate*, **28 (20)**, 8078–8092, doi:10.1175/JCLI-D-15-0369.1.

724 Cess, R. D., and S. D. Goldenberg, 1981: The effect of ocean heat capacity upon global warming
725 due to increasing atmospheric carbon dioxide. *Journal of Geophysical Research*, **86 (80)**, 498–
726 502.

727 Charney, J., W. J. Quirk, S.-H. Chow, and J. Kornfield, 1977: A comparative study of the effects
728 of albedo change on drought in semi-arid regions. doi:10.1175/1520-0469(1977)034<1366:
729 ACSOTE>2.0.CO;2.

- 730 Charney, J., P. H. Stone, and W. J. Quirk, 1975: Drought in Sahara - Biogeophysical Feedback
731 Mechanism. *Science*, **187 (4175)**, 434–435, doi:doi:10.1126/science.187.4175.434.
- 732 Chiang, J. C. H., and C. M. Bitz, 2005: Influence of high latitude ice cover on the marine Intertrop-
733 ical Convergence Zone. *Climate Dynamics*, **25 (5)**, 477–496, doi:10.1007/s00382-005-0040-5.
- 734 Cvijanovic, I., and J. C. Chiang, 2013: Global energy budget changes to high latitude North
735 Atlantic cooling and the tropical ITCZ response. *Climate Dynamics*, **40 (5-6)**, 1435–1452, doi:
736 10.1007/s00382-012-1482-1.
- 737 Davin, E. L., N. de Noblet-Ducoudré, N. de Noblet-Ducoudre, and N. de Noblet-Ducoudré, 2010:
738 Climatic Impact of Global-Scale Deforestation: Radiative versus Nonradiative Processes. *Jour-
739 nal of Climate*, **23 (1)**, 97–112, doi:10.1175/2009JCLI3102.1, URL [http://journals.ametsoc.org/
740 doi/abs/10.1175/2009JCLI3102.1](http://journals.ametsoc.org/doi/abs/10.1175/2009JCLI3102.1).
- 741 Devaraju, N., N. de Noblet-Ducoudré, B. Quesada, and G. Bala, 2018: Quantifying the relative
742 importance of direct and indirect biophysical effects of deforestation on surface temperature and
743 teleconnections. *Journal of Climate*, **31 (10)**, 3811–3829, doi:10.1175/JCLI-D-17-0563.1.
- 744 Dickinson, R. E., 1983: Land surface processes and climate—surface albedos and energy balance.
745 *Advances in Geophysics*, **25 (C)**, 305–353, doi:10.1016/S0065-2687(08)60176-4.
- 746 Donohoe, A., and D. S. Battisti, 2011: Atmospheric and surface contributions to planetary albedo.
747 *Journal of Climate*, **24 (16)**, 4402–4418, doi:10.1175/2011JCLI3946.1.
- 748 Donohoe, A., J. Marshall, D. Ferreira, and D. Mcgee, 2013: The relationship between ITCZ
749 location and cross-equatorial atmospheric heat transport: From the seasonal cycle to the last
750 glacial maximum. *Journal of Climate*, **26 (11)**, 3597–3618, doi:10.1175/JCLI-D-12-00467.1.

- 751 Flanner, M. G., K. M. Shell, M. Barlage, D. K. Perovich, and M. A. Tschudi, 2011: Radiative
752 forcing and albedo feedback from the Northern Hemisphere cryosphere between 1979 and 2008.
753 *Nature Geoscience*, **4** (3), 151–155, doi:10.1038/ngeo1062.
- 754 Geen, R., S. Bordoni, D. Battisti, and K. Hui, 2020: The Dynamics of the Global Monsoon -
755 Connecting Theory and Observations. *Earth and Space Science Open Archive*, 1–26, doi:https:
756 //doi.org/10.1002/essoar.10502409.1.
- 757 Hurrell, J. W., and Coauthors, 2013: The Community Earth System Model: A Framework for
758 Collaborative Research. *Bulletin of the American Meteorological Society*, **94** (9), 1339–1360,
759 doi:10.1175/BAMS-D-12-00121.1, URL <https://doi.org/10.1175/BAMS-D-12-00121.1>.
- 760 Kang, S. M., 2020: Extratropical Influence on the Tropical Rainfall Distribution. **1**, 24–36.
- 761 Kang, S. M., D. M. W. Frierson, and I. M. Held, 2009: The Tropical Response to Extrat-
762 ropical Thermal Forcing in an Idealized GCM: The Importance of Radiative Feedbacks and
763 Convective Parameterization. *Journal of the Atmospheric Sciences*, **66** (9), 2812–2827, doi:
764 10.1175/2009JAS2924.1.
- 765 Kang, S. M., I. M. Held, D. M. W. Frierson, and M. Zhao, 2008: The Response of the ITCZ
766 to Extratropical Thermal Forcing: Idealized Slab-Ocean Experiments with a GCM. *Journal of*
767 *Climate*, **21** (14), 3521–3532, doi:10.1175/2007JCLI2146.1.
- 768 Kooperman, G. J., Y. Chen, F. M. Hoffman, C. D. Koven, K. Lindsay, M. S. Pritchard, A. L.
769 Swann, and J. T. Randerson, 2018: Forest response to rising CO₂ drives zonally asymmet-
770 ric rainfall change over tropical land. *Nature Climate Change*, **8** (5), 434–440, doi:10.1038/
771 s41558-018-0144-7, URL <http://dx.doi.org/10.1038/s41558-018-0144-7>.

- 772 Koster, R., and Coauthors, 2004: Regions of Strong Coupling Between Soil Moisture and Precip-
773 itation. *Science*, **305**, 1138–1140.
- 774 Koster, R. D., and Coauthors, 2006: GLACE: The Global Land-Atmosphere Coupling Experi-
775 ment. Part I: Overview. *Journal of Hydrometeorology*, **7** (4), 590–610, doi:10.1175/JHM510.1.
- 776 Laguë, M. M., G. B. Bonan, and A. L. S. Swann, 2019: Separating the Impact of Individual
777 Land Surface Properties on the Terrestrial Surface Energy Budget in both the Coupled and
778 Uncoupled Land–Atmosphere System. *Journal of Climate*, **32** (18), 5725–5744, doi:10.1175/
779 jcli-d-18-0812.1.
- 780 Laguë, M. M., and A. L. S. Swann, 2016: Progressive Mid-latitude Afforestation: Impacts on
781 Clouds, Global Energy Transport, and Precipitation. *Journal of Climate*, **29** (15), 5561–5573,
782 doi:10.1175/JCLI-D-15-0748.1, URL <http://dx.doi.org/10.1175/JCLI-D-15-0748.1>.
- 783 Lawrence, D. M., and Coauthors, 2019: The Community Land Model Version 5: Description
784 of New Features, Benchmarking, and Impact of Forcing Uncertainty. *Journal of Advances in*
785 *Modeling Earth Systems*, **11** (12), 4245–4287, doi:10.1029/2018MS001583.
- 786 Lee, X., and Coauthors, 2011: Observed increase in local cooling effect of deforestation at higher
787 latitudes. *Nature*, **479** (7373), 384–387, doi:10.1038/nature10588, URL [http://dx.doi.org/10.](http://dx.doi.org/10.1038/nature10588)
788 [1038/nature10588](http://dx.doi.org/10.1038/nature10588).
- 789 Lintner, B. R., A. B. Gilliland, and I. Y. Fung, 2004: Mechanisms of convection-induced modula-
790 tion of passive tracer interhemispheric transport interannual variability. *Journal of Geophysical*
791 *Research D: Atmospheres*, **109** (13), 1–13, doi:10.1029/2003JD004306.

792 Manabe, S., 1969: Climate and the Ocean Circulation 1. *Monthly Weather Review*, **97 (11)**, 739–
793 774, doi:10.1175/1520-0493(1969)097<0739:CATOC>2.3.CO;2, URL [http://journals.ametsoc.
794 org/doi/abs/10.1175/1520-0493\(1969\)097%3C0739:CATOC%3E2.3.CO;2](http://journals.ametsoc.org/doi/abs/10.1175/1520-0493(1969)097%3C0739:CATOC%3E2.3.CO;2).

795 Milly, P. C. D., and a. B. Shmakin, 2002: Global Modeling of Land Water and Energy Balances.
796 Part I: The Land Dynamics (LaD) Model. *Journal of Hydrometeorology*, **3 (3)**, 283–299, doi:10.
797 1175/1525-7541(2002)003<0283:GMOLWA>2.0.CO;2, URL [http://journals.ametsoc.org/doi/
798 abs/10.1175/1525-7541%282002%29003%3C0283%3AGMOLWA%3E2.0.CO%3B2](http://journals.ametsoc.org/doi/abs/10.1175/1525-7541%282002%29003%3C0283%3AGMOLWA%3E2.0.CO%3B2).

799 Neale, R. B., and Coauthors, 2012: Description of the NCAR community atmosphere model
800 (CAM 5.0). *NCAR Tech. Note NCAR/TN-486+STR*.

801 North, G. R., J. G. Mengel, and D. A. Short, 1983: Simple energy balance model resolving the
802 seasons and the continents: application to the astronomical theory of the ice ages. *Journal of
803 Geophysical Research*, **88 (C11)**, 6576–6586, doi:10.1029/JC088iC11p06576.

804 Oleson, K. W., and Coauthors, 2013: Technical Description of version 4.5 of the Community
805 Land Model (CLM). *NCAR Tech. Note NCAR/TN-503+STR*, (**July**), NCAR/TN-503+STR,
806 URL http://www.cesm.ucar.edu/models/cesm1.2/clm/CLM45_Tech_Note.pdf[http://www.cesm.
807 ucar.edu/models/cesm1.2/clm/](http://www.cesm.ucar.edu/models/cesm1.2/clm/).

808 Payne, R. E., 1972: Albedo of the Sea Surface. 959–970 pp., doi:10.1175/1520-0469(1972)
809 029<0959:aotss>2.0.co;2.

810 Pendergrass, A. G., A. Conley, and F. M. Vitt, 2018: Surface and top-of-Atmosphere radiative
811 feedback kernels for cesm-cam5. *Earth System Science Data*, **10 (1)**, 317–324, doi:10.5194/
812 essd-10-317-2018.

- 813 Peterson, H. G., and W. R. Boos, 2020: Feedbacks and eddy diffusivity in an energy balance
814 model of tropical rainfall shifts. *npj Climate and Atmospheric Science*, **3** (1), 1–10, doi:10.
815 1038/s41612-020-0114-4, URL <http://dx.doi.org/10.1038/s41612-020-0114-4>.
- 816 Sellers, P. J., and Coauthors, 1996: Comparison of radiative and physiological effects of dou-
817 bled atmospheric CO₂ on climate. *SCIENCE-NEW YORK THEN WASHINGTON-*, **271** (5254),
818 1402–1405, doi:10.1126/science.271.5254.1402.
- 819 Shell, K. M., J. T. Kiehl, and C. A. Shields, 2008: Using the radiative kernel technique to calculate
820 climate feedbacks in NCAR’s Community Atmospheric Model. *Journal of Climate*, **21** (10),
821 2269–2282, doi:10.1175/2007JCLI2044.1.
- 822 Shukla, J., and Y. Mintz, 1982: Influence of Land-Surface Evapotranspiration on the Earth’s Cli-
823 mate. *Science*, **215** (4539), 1498–1501.
- 824 Soden, B. J., and I. M. Held, 2006: An Assessment of Climate Feedbacks in Coupled Ocean–
825 Atmosphere Models. *Journal of Climate*, **19** (14), 3354–3360, doi:10.1175/JCLI3799.1, URL
826 <http://dx.doi.org/10.1175/JCLI3799.1>.
- 827 Soden, B. J., I. M. Held, R. Colman, K. M. Shell, J. T. Kiehl, and C. A. Shields, 2008: Quantifying
828 Climate Feedbacks Using Radiative Kernels. *Journal of Climate*, **21** (14), 3504–3520, doi:10.
829 1175/2007JCLI2110.1, URL <http://journals.ametsoc.org/doi/abs/10.1175/2007JCLI2110.1>
830 <http://dx.doi.org/10.1175/2007JCLI2110.1>.
- 831 Stocker, T. F., and Coauthors, 2013: Climate change 2013 the physical science basis: Working
832 Group I contribution to the fifth assessment report of the Intergovernmental Panel on Climate
833 Change. *Contribution of Working Group I to the Fifth Assessment Report of the Intergovern-
834 mental Panel on Climate Change.*, **9781107057**, 1–1535, doi:10.1017/CBO9781107415324.

- 835 Swann, A. L. S., I. Y. Fung, and J. C. H. Chiang, 2012: Mid-latitude afforestation shifts general
836 circulation and tropical precipitation. *Proceedings of the National Academy of Sciences*, **109** (3),
837 712–716, doi:10.1073/pnas.1116706108.
- 838 Winckler, J., and Coauthors, 2018: Different response of surface temperature and air temperature
839 to deforestation in climate models. *Earth System Dynamics Discussions*, 1–17, doi:10.5194/
840 esd-2018-66.
- 841 Zarakas, C. M., A. L. Swann, M. M. Laguë, K. C. Armour, and J. T. Randerson, 2020: Plant
842 Physiology Increases the Magnitude and Spread of the Transient Climate Response to CO₂ in
843 CMIP6 Earth System Models. *Journal of Climate*, 1–44, doi:10.1175/jcli-d-20-0078.1.
- 844 Zelinka, M. D., D. A. Randall, M. J. Webb, and S. A. Klein, 2017: Clearing clouds of uncertainty.
845 *Nature Climate Change*, **7** (10), 674–678, doi:10.1038/nclimate3402.

846 **LIST OF TABLES**

847 **Table 1.** Table of the globally averaged annual mean (and standard deviation) of the
848 components of the TOA energy budget breakdown. Mean values are bold where
849 they exceed the standard deviation. All fluxes in this table are considered posi-
850 tive downwards, such that a positive (negative) value means a net gain (loss) of
851 energy at the TOA due to each component. 41

852 **Table 2.** Pattern correlation between the TOA energy budget response to each individual
853 forcing and feedback term, calculated using the area-weighted Pearson-r cor-
854 relation coefficient. Note that (a) this only accounts for correlation between the
855 *pattern* of the TOA response to each surface property, and not the intensity, and
856 (b) the imposed albedo change is zero everywhere for a change in land surface
857 evaporative resistance. 42

Decrease in land albedo:											
	$dTOA_{net}$	$dSW_{TOA,net}$	$dLW_{TOA,net}$	dSW_{α_i}	dSW_{α_s}	dSW_q	dLW_q	dLW_{T_s}	dLW_T	dSW_{clouds}	dLW_{clouds}
mean	0.08	2.03	-1.95	1.60	0.52	0.42	2.03	-0.72	-2.77	-0.51	-0.49
std	0.65	0.38	0.39	0.04	0.10	0.05	0.26	0.06	0.55	0.37	0.21
Increase in land evaporative resistance											
	$dTOA_{net}$	dSW_{model}	dLW_{model}	dSW_{α_i}	dSW_{α_s}	dSW_q	dLW_q	dLW_{T_s}	dLW_T	dSW_{clouds}	dLW_{clouds}
mean	0.04	0.85	-0.81	0	0.15	0.18	0.97	-0.27	-0.8	0.52	-0.70
std	0.62	0.4	0.37	0	0.08	0.05	0.26	0.06	0.53	0.41	0.19

858 TABLE 1. Table of the globally averaged annual mean (and standard deviation) of the components of the TOA
859 energy budget breakdown. Mean values are bold where they exceed the standard deviation. All fluxes in this
860 table are considered positive downwards, such that a positive (negative) value means a net gain (loss) of energy
861 at the TOA due to each component.

TOA Breakdown Term	Pattern Correlation
Albedo (Snow/Ice)	0.38
SW Water Vapour	0.87
LW Water Vapour	0.89
LW from Surface Temperature	0.73
LW from Column Air Temperature	0.87
SW Cloud Effects	0.37
LW Cloud Effect	0.52
Total TOA <i>SW</i> Response	0.48
Total TOA <i>LW</i> Response	0.52
Total TOA net Response	0.33

862 TABLE 2. Pattern correlation between the TOA energy budget response to each individual forcing and feed-
863 back term, calculated using the area-weighted Pearson-r correlation coefficient. Note that (a) this only accounts
864 for correlation between the *pattern* of the TOA response to each surface property, and not the intensity, and (b)
865 the imposed albedo change is zero everywhere for a change in land surface evaporative resistance.

866 **LIST OF FIGURES**

867 **Fig. 1.** Total change in net TOA $SW + LW$ as a result of decreasing land albedo (left column) and
868 increasing land evaporative resistance (right column) for (a) the annual mean, (b) June-July-
869 August, and (c) December-January-February. The global mean value [W/m^2] of the change
870 in net TOA radiation is noted to the lower left of each panel. Only values that differ with
871 $p < 0.05$ in a students' t-test are shown. 45

872 **Fig. 2.** Map (and zonal average) of the change in annual mean precipitation for (a) a 0.1 decrease in
873 land surface albedo and (b) a 100 s/m increase in land surface evaporative resistance. Only
874 values with $p < 0.05$ in a student's t-test are shown for the maps. 46

875 **Fig. 3.** Change in annual mean net top of atmosphere energy fluxes [W/m^2] as a result of decreasing
876 land surface albedo. All fluxes (SW and LW) are shown positive down such that red colours
877 indicate more energy absorbed by the Earth system, while blue colours indicate more energy
878 lost by the Earth system. (a) shows the change in TOA net SW radiation from the imposed
879 change in albedo. (b) shows change in TOA net SW radiation from albedo changes to do
880 changes in snow and ice. (c) and (d) show, respectively, changes in TOA SW and LW radi-
881 ation from changes in column water vapour. (e) shows change in TOA LW from combined
882 changes in the surface radiative temperature and changes in air temperature. (f) shows the
883 total change in TOA $SW + LW$ from changes in cloud cover. The effect of cloud cover is
884 separated into its impact on TOA SW in (g) and TOA LW in (h). The area-weighted global
885 mean value for each term is shown to the lower left of each map. Only values that differ
886 with $p < 0.05$ in a students' t-test are shown. 47

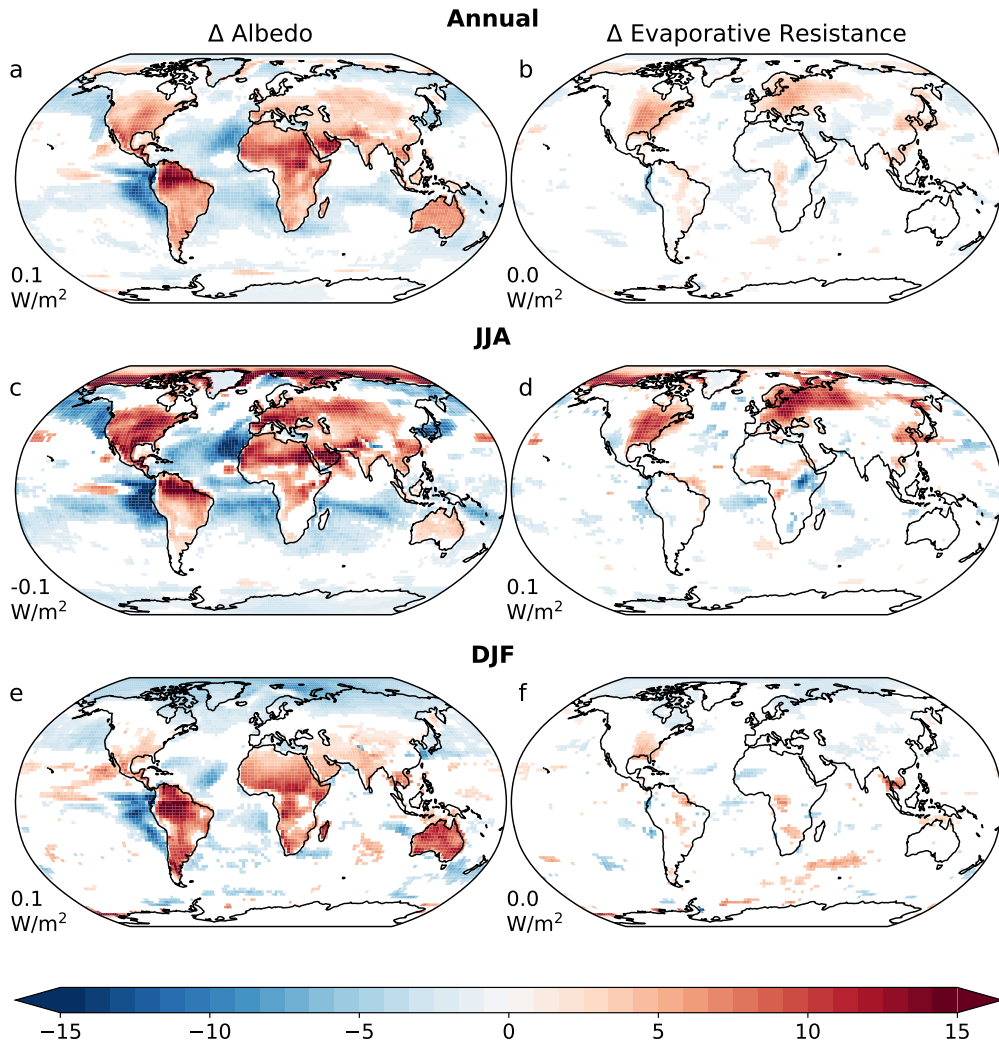
887 **Fig. 4.** Same as figure 3, but for an increase in land surface evaporative resistance. Note that in this
888 case, there is no imposed change in land surface albedo. 48

889 **Fig. 5.** Relationship between the zonal-mean latitude of the ITCZ (measured as the center of mass
890 of tropical precipitation ϕ_p) and the magnitude of cross-equatorial energy flux (in PW).
891 The relationship is shown for (a) the annual mean, (b) December/January/February, and
892 (c) June/July/August. Each small dot represents the annual average of a single year from
893 5 30-year model runs: a "baseline" simulation with a global land albedo of $\alpha = 0.2$ and
894 evaporative resistance of $r_s = 100s/m$, a dark land simulation with $\alpha = 0.1$, a bright land
895 simulation with $\alpha = 0.3$, a high evaporative resistance run with $r_s = 200$ s/m, and a low
896 evaporative resistance run with $r_s = 30$ s/m. The large grey circle shows the multi-year
897 average of the baseline ($\alpha = 0.2$, $r_s = 100s/m$) simulation, while the black square and red
898 triangle show the multi-year average of the dark ($\alpha = 0.1$) and high evaporative resistance
899 ($r_s = 200$ s/m) simulations, respectively. The slope of the linear relationship between cross-
900 equatorial atmospheric energy transport calculated using the TOA energy imbalance and
901 the ITCZ location is noted in the upper right of each panel, while the same relationship
902 calculated using vertically integrated moist static energy and meridional winds is noted in
903 brackets. 49

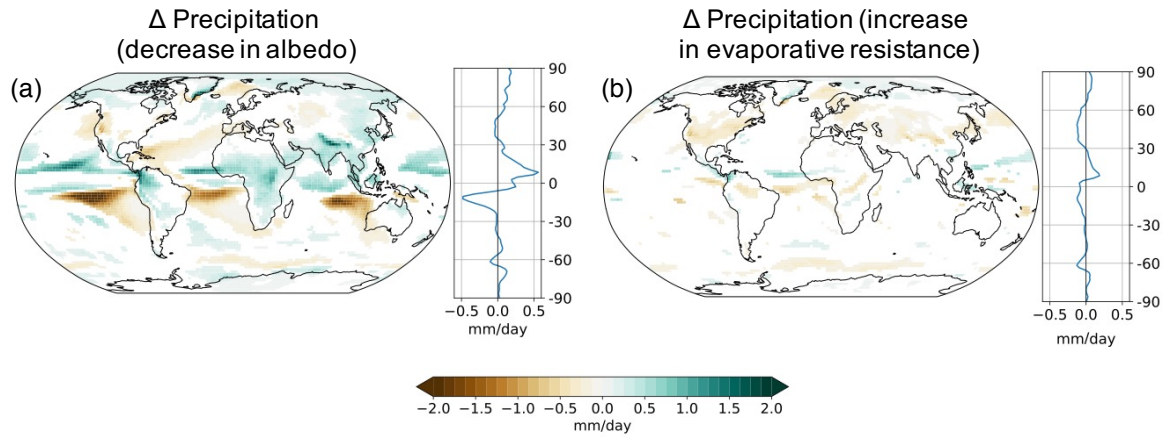
904 **Fig. 6.** The breakdown of the change in the zonally averaged annual mean location the ITCZ (mea-
905 sured by ϕ_p) resulting from each component, re-scaled to a 1° total northwards shift. Solid
906 (hatched) bars show the change in the zonal mean ITCZ location for a uniform decrease
907 of land surface albedo (increase of evaporative resistance). From left to right, bars show:
908 the total modelled change (dark grey); the change due to the sum of all of the individual
909 components (light grey); the change attributable to the imposed change in albedo (orange),
910 the change in albedo due to changes in snow and ice (yellow), LW effects due to changes
911 in surface temperature (dark purple), LW effects to due vertical changes in the atmospheric
912 temperature profile (lilac), SW changes due to changes in water vapour (light green), LW

913 changes due to changes in water vapour (dark green), *SW* changes due to changes in cloud
914 cover (light blue), and *LW* changes due to changes in cloud cover (dark blue). The magni-
915 tude of the ITCZ shift is noted above each bar, as well as the *p* value taken from a students'
916 t-test, where $p < 0.05$ indicates a significant shift from the baseline simulation. 50

Net TOA SW + LW

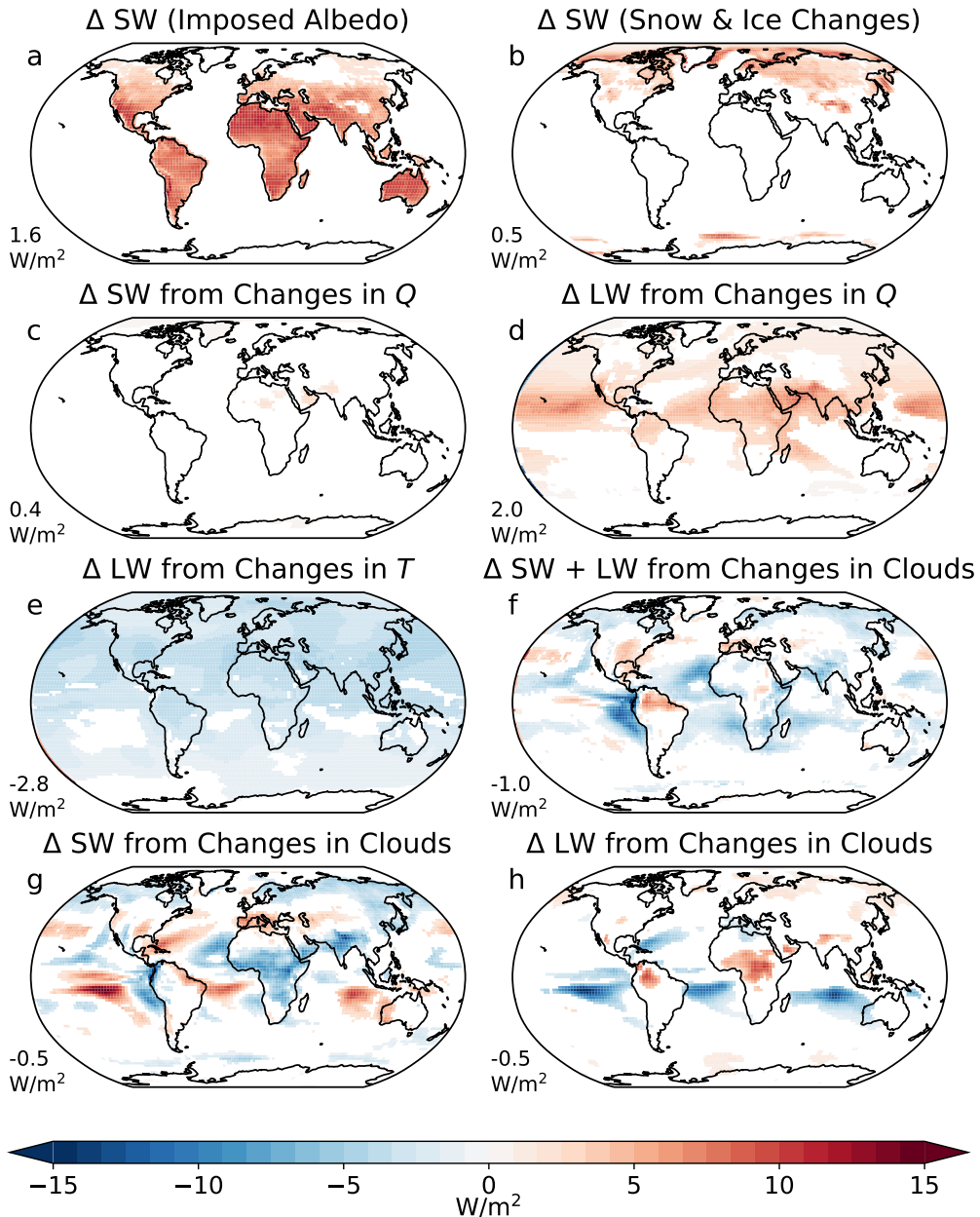


917 FIG. 1. Total change in net TOA $SW + LW$ as a result of decreasing land albedo (left column) and increasing
918 land evaporative resistance (right column) for (a) the annual mean, (b) June-July-August, and (c) December-
919 January-February. The global mean value [W/m^2] of the change in net TOA radiation is noted to the lower left
920 of each panel. Only values that differ with $p < 0.05$ in a student's t-test are shown.



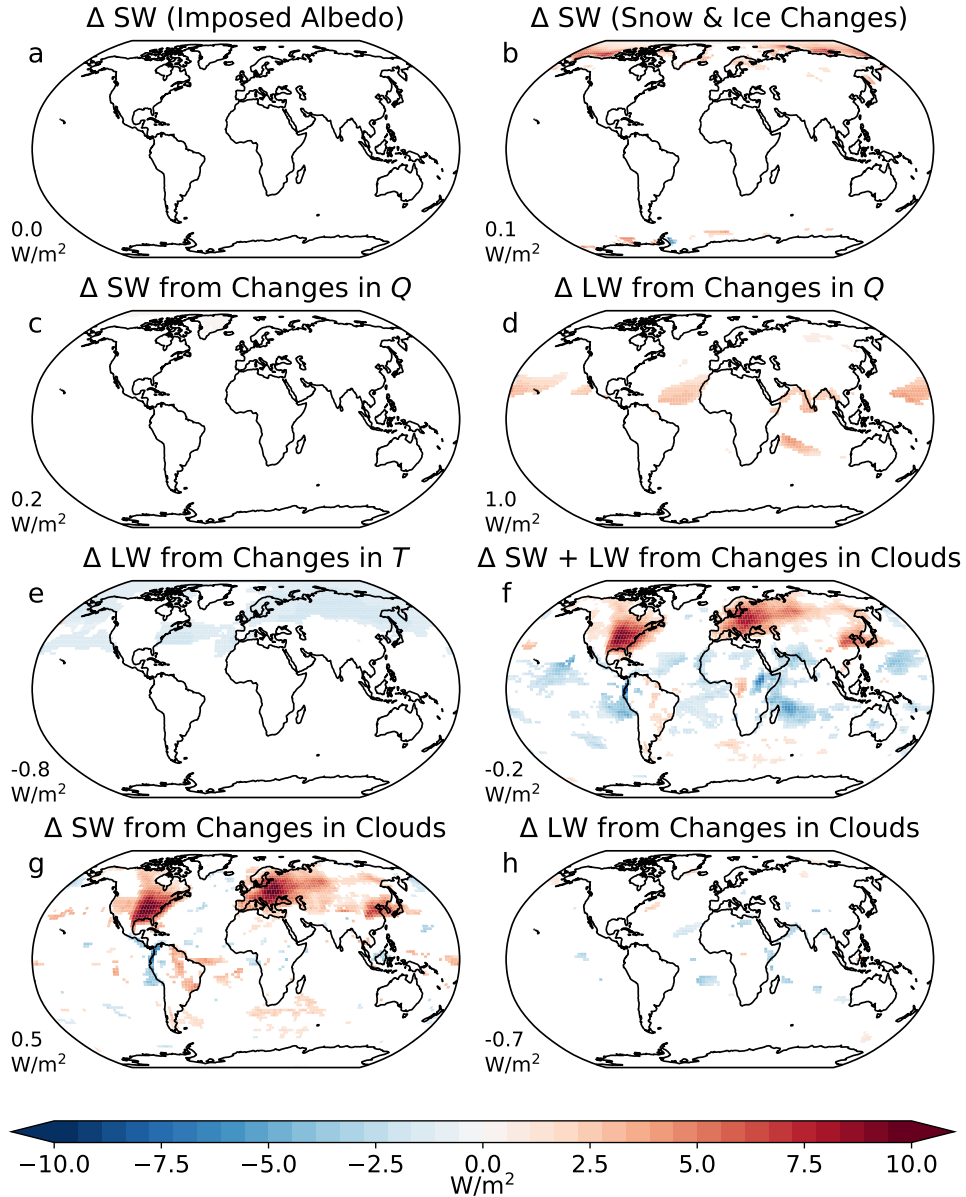
921 FIG. 2. Map (and zonal average) of the change in annual mean precipitation for (a) a 0.1 decrease in land
 922 surface albedo and (b) a 100 s/m increase in land surface evaporative resistance. Only values with $p < 0.05$ in a
 923 student's t-test are shown for the maps.

**Net TOA flux breakdown, decrease in land albedo
ANN**



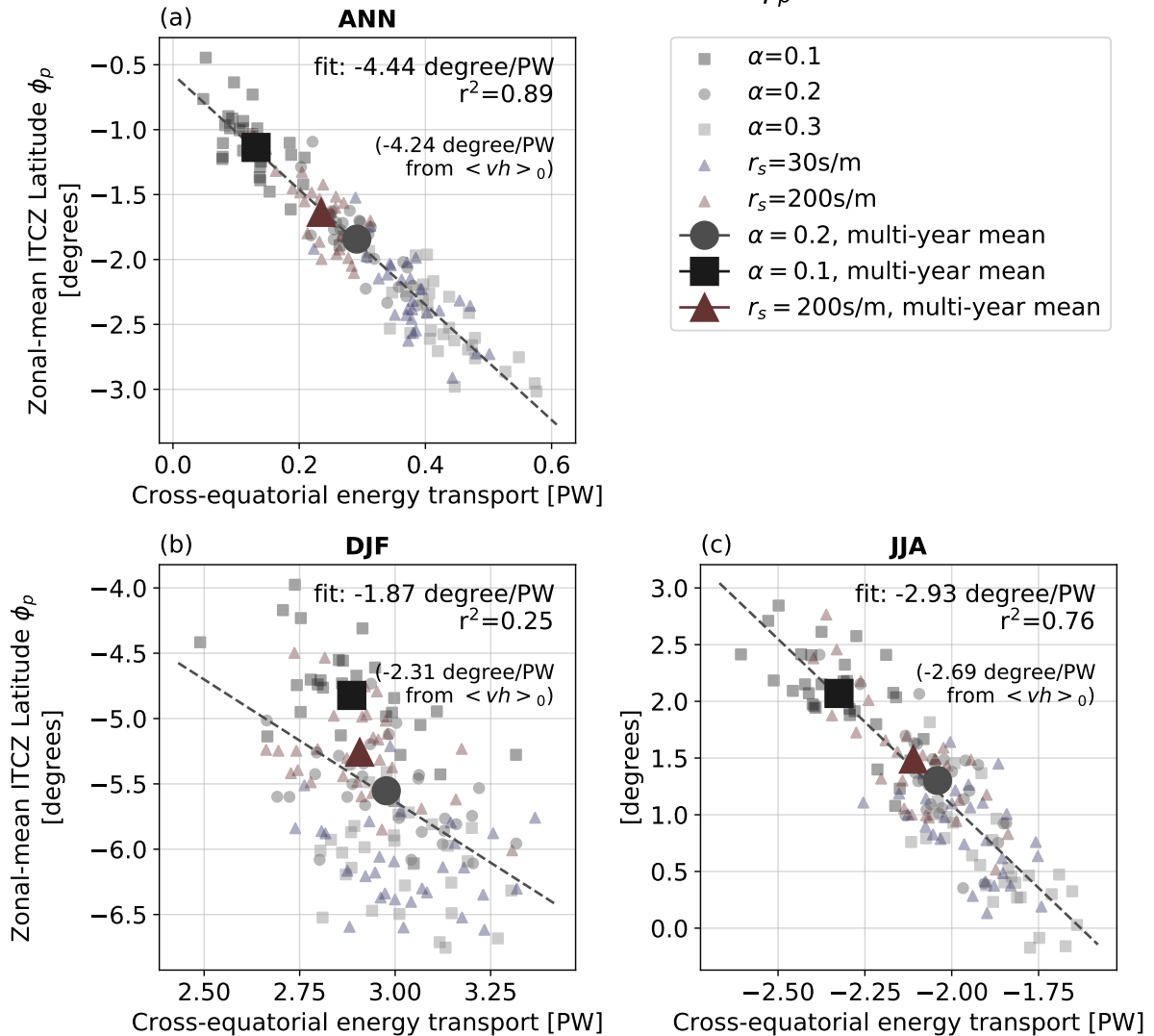
924 FIG. 3. Change in annual mean net top of atmosphere energy fluxes [W/m^2] as a result of decreasing land
 925 surface albedo. All fluxes (SW and LW) are shown positive down such that red colours indicate more energy
 926 absorbed by the Earth system, while blue colours indicate more energy lost by the Earth system. (a) shows the
 927 change in TOA net SW radiation from the imposed change in albedo. (b) shows change in TOA net SW radiation
 928 from albedo changes to do changes in snow and ice. (c) and (d) show, respectively, changes in TOA SW and LW
 929 radiation from changes in column water vapour. (e) shows change in TOA LW from combined changes in the
 930 surface radiative temperature and changes in air temperature. (f) shows the total change in TOA SW + LW from
 931 changes in cloud cover. The effect of cloud cover is separated into its impact on TOA SW in (g) and TOA LW
 932 in (h). The area-weighted global mean value for each term is shown to the lower left of each map. Only values

**Net TOA flux breakdown, increase in land evaporative resistance
(ANN)**



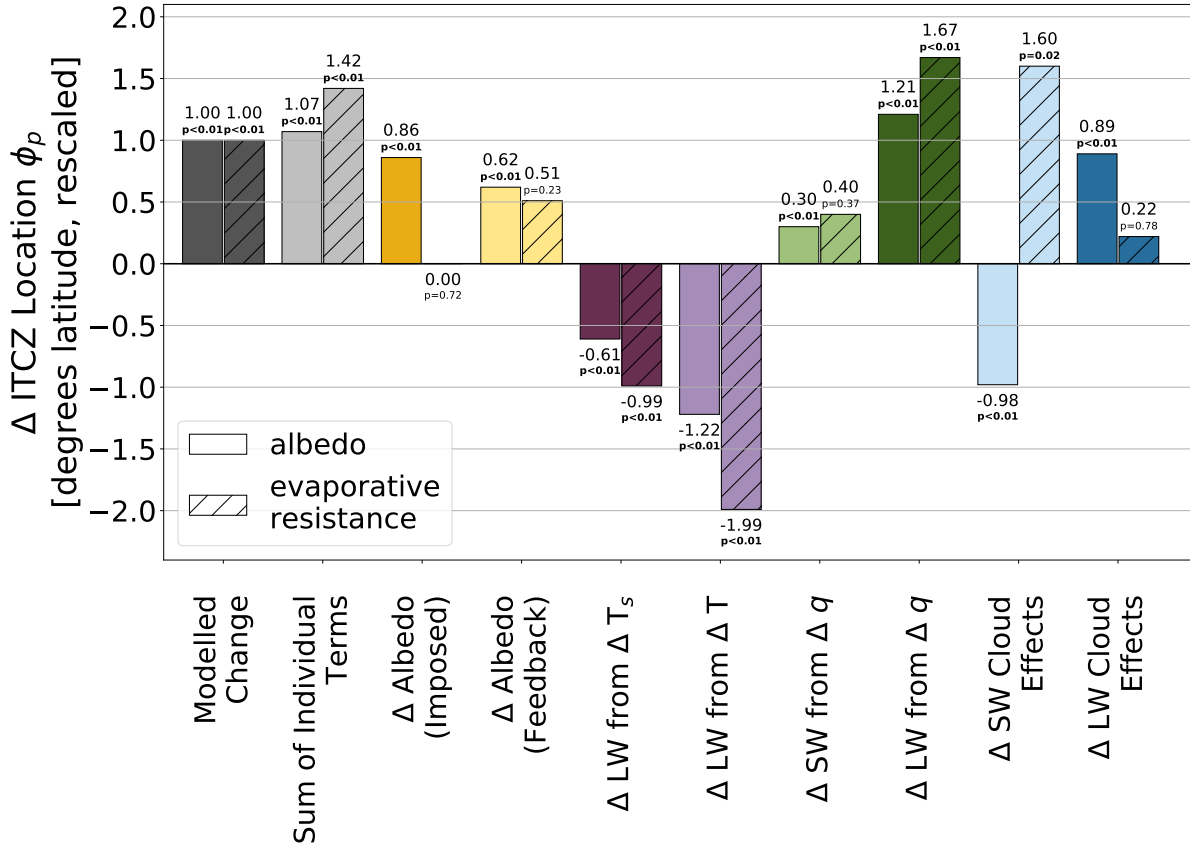
934 FIG. 4. Same as figure 3, but for an increase in land surface evaporative resistance. Note that in this case,
935 there is no imposed change in land surface albedo.

Cross-equatorial Atmospheric Energy Transport vs. ITCZ Latitude ϕ_p



936 FIG. 5. Relationship between the zonal-mean latitude of the ITCZ (measured as the center of mass of tropical
 937 precipitation ϕ_p) and the magnitude of cross-equatorial energy flux (in PW). The relationship is shown for (a) the
 938 annual mean, (b) December/January/February, and (c) June/July/August. Each small dot represents the annual
 939 average of a single year from 5 30-year model runs: a “baseline” simulation with a global land albedo of $\alpha = 0.2$
 940 and evaporative resistance of $r_s = 100\text{s/m}$, a dark land simulation with $\alpha = 0.1$, a bright land simulation with
 941 $\alpha = 0.3$, a high evaporative resistance run with $r_s = 200\text{ s/m}$, and a low evaporative resistance run with $r_s = 30$
 942 s/m . The large grey circle shows the multi-year average of the baseline ($\alpha = 0.2$, $r_s = 100\text{s/m}$) simulation,
 943 while the black square and red triangle show the multi-year average of the dark ($\alpha = 0.1$) and high evaporative
 944 resistance ($r_s = 200\text{ s/m}$) simulations, respectively. The slope of the linear relationship between cross-equatorial
 945 atmospheric energy transport calculated using the TOA energy imbalance and the ITCZ location is noted in the
 946 upper right of each panel, while the same relationship calculated using vertically integrated moist static energy
 947 and meridional winds is noted in brackets.

Attribution of Δ ITCZ Location ϕ_p from Each TOA Breakdown Component (ANN)



948 FIG. 6. The breakdown of the change in the zonally averaged annual mean location the ITCZ (measured
 949 by ϕ_p) resulting from each component, re-scaled to a 1° total northwards shift. Solid (hatched) bars show the
 950 change in the zonal mean ITCZ location for a uniform decrease of land surface albedo (increase of evaporative
 951 resistance). From left to right, bars show: the total modelled change (dark grey); the change due to the sum of
 952 all of the individual components (light gray); the change attributable to the imposed change in albedo (orange),
 953 the change in albedo due to changes in snow and ice (yellow), LW effects due to changes in surface temperature
 954 (dark purple), LW effects to due vertical changes in the atmospheric temperature profile (lilac), SW changes due
 955 to changes in water vapour (light green), LW changes due to changes in water vapour (dark green), SW changes
 956 due to changes in cloud cover (light blue), and LW changes due to changes in cloud cover (dark blue). The
 957 magnitude of the ITCZ shift is noted above each bar, as well as the p value taken from a student's t-test, where
 958 $p < 0.05$ indicates a significant shift from the baseline simulation.